Journal of Cosmology
and Astroparticle
Physics

SISSA

PAPER • OPEN ACCESS

Morphological signatures of gravitational evolution, redshift-space distortions, and massive neutrinos in large-scale structure

To cite this article: Priya Goyal *et al* JCAP08(2026)082

View the article online for updates and enhancements.

You may also like

- Probing massive neutrinos with the Minkowski functionals of large-scale structure
Wei Liu, Aoxiang Jiang and Wenjuan Fang
- Probing massive neutrinos and modified gravity with redshift-space morphologies and anisotropies of large-scale structure
Wei Liu, Liang Wu, Francisco Villaescusa-Navarro et al.
- Cosmological Parameter Estimation from the Two-dimensional Genus Topology—Measuring the Expansion History Using the Genus Amplitude as a Standard Ruler
Stephen Appleby, Changbom Park, Sungwook E. Hong et al.

This content was downloaded from IP address 14.139.159.162 on 17/10/2026 at 07:30

Journal of Cosmology and Astroparticle Physics
An IOP and SISSA journal

Received: *March 28, 2026*
Revised: *June 15, 2026*
Accepted: *July 15, 2026*
Published: *August 28, 2026*

Morphological signatures of gravitational evolution, redshift-space distortions, and massive neutrinos in large-scale structure

Priya Goyal[a], **Stephen Appleby**[a,b,c], **Pravabati Chingangbam**[d] and **Changbom Park**[a]

[a] *Korea Institute for Advanced Study (KIAS), 85 Hoegiro, Dongdaemun-gu, Seoul 02455, Republic of Korea*
[b] *Asia Pacific Center for Theoretical Physics, Pohang 37673, Republic of Korea*
[c] *Department of Physics, POSTECH, Pohang 37673, Republic of Korea*
[d] *Indian Institute of Astrophysics, Koramangala II Block, Bangalore 560 034, India*
E-mail: priyagoyal@kias.re.kr, stephen@kias.re.kr, prava@iiap.res.in, cbp@kias.re.kr

Abstract: We investigate the morphological properties of large-scale structure in the Universe and the physical processes that modify the excursion-set morphology of the three-dimensional matter density field. Using the Quijote N-body simulation suite, we study how an initially Gaussian random matter density field is altered by non-linear gravitational evolution, redshift-space distortions, and massive neutrino free-streaming. To quantify these effects, we employ a comprehensive set of morphological descriptors, including Minkowski Functionals, Betti numbers, Minkowski Tensors, and local measures of the size and shape of connected components and cavities. We find that gravitational evolution, on quasi-linear scales $R_G \sim 10\,h^{-1}\,\mathrm{Mpc}$, strongly skews the one-point distribution and slightly smooths the field via the merging of critical points, with a more pronounced effect for minima and wall saddle points than for peaks. Redshift-space distortions produce the strongest morphological signal, generating pronounced anisotropies that are robustly captured by Minkowski Tensors and local shape measures, arising from both coherent large-scale flows and non-linear Finger-of-God effects. In contrast, massive neutrinos induce an approximately isotropic suppression of small-scale structure, slightly reducing the amplitudes of the Minkowski Functionals while leaving individual shape measures largely unchanged. We further explore the sensitivity of these statistics to variations in cosmological parameters Ω_m, n_s, and σ_8, finding that they probe strongly degenerate combinations of Ω_m and n_s, while also exhibiting sensitivity to σ_8 through the non-Gaussianity of the evolved density field.

Keywords: cosmological simulations, non-gaussianity, cosmic web, cosmological neutrinos

ArXiv ePrint: 2603.19734

© 2026 The Author(s). Published by IOP Publishing Ltd on behalf of Sissa Medialab. Original content from this work may be used under the terms of the Creative Commons Attribution 4.0 licence. Any further distribution of this work must maintain attribution to the author(s) and the title of the work, journal citation and DOI.

https://doi.org/10.1088/1475-7516/2026/08/082

JCAP08(2026)082

Contents

1 Introduction **1**

2 Data and methodology **3**
2.1 Data 3
2.2 Minkowski Functionals, Betti numbers, Minkowski Tensors 4

3 Morphology of excursion sets for GRF **7**

4 Gravitational evolution **10**

5 Redshift space distortion **13**
5.1 Linear RSD 14
5.2 Non-linear RSD 16

6 Neutrino mass **18**

7 Galaxy bias **19**

8 Shot noise **20**

9 Parameter sensitivity **22**

10 Discussion **27**
10.1 Summary of results 27
10.2 Comparison with previous work 28
10.3 Sensitivity of morphological statistics to cosmology 29
10.4 Limitations & future work 30

A Effect of gravitational evolution **30**

B Information content of the local statistics **30**

C High threshold ensemble average **34**
C.1 Local shape information 36

JCAP08(2026)082

1 Introduction

The large-scale structures (LSS) in the Universe contains a wealth of cosmological information. As primordial density fluctuations evolve under gravitational instability, they form the complex web of clusters, filaments, walls, and voids observed in the present-day matter distribution. The cosmological information is encoded in the statistical properties of the LSS, which is typically extracted using the power spectrum (and its Fourier counterpart, correlation function) [1] and higher N-point functions. To probe the non-linear and non-Gaussian regime of structure formation, higher-order statistics [1, 2] and geometrical descriptors [3–7] are

increasingly utilized. One such approach is to study the morphology of excursion sets of the field, characterising them by their geometrical and topological properties.

Topological measures like the genus, which quantifies the connectivity of iso-density or iso-temperature contour surfaces of smooth matter density or the cosmic microwave temperature field, and the Betti numbers, which are the counts of individual connected components and cavities, have long been utilized to probe primordial non-gaussianity [8–11], reconstruct expansion history of the universe [12, 13] and constrain models of galaxy formation and cosmological parameters [14–18]. Alongside topology, the geometry of excursion sets is often characterized using Minkowski functionals (MFs) which provide information on the statistical properties of the field and the physical processes that shape it [3, 4, 11, 19–53]. In addition to MFs, the Minkowski Tensors (MTs) are their tensorial generalisation, extend the morphological analysis by capturing directional and anisotropic information of the field. MTs are defined as integrals over the boundary of an excursion set, with integrands proportional to symmetric tensor products of position vectors and normals to the boundary [5, 7, 54–58]. The ensemble average of the MTs measured from Gaussian, isotropic and anisotropic random fields, were derived in [59–61]. Further, authors in [62] analytically calculated expected MTs of arbitrary rank for the level sets of Gaussian random fields. Numerical methods with which to extract the MTs from random fields can be found in [5, 63–65]. These statistics were first applied to cosmological data in [66], where a significant anisotropic signal was found in the 2015 E-mode Planck data. Subsequently, they were employed to investigate different cosmological fields including CMB temperature and polarization fields [21, 67–70], 21 cm brightness temperature field from reionization epochs [71, 72], CMB foregrounds like synchrotron radiation and dust emission [51, 73] among many. In addition, authors have written a series of papers on the application of the MTs to the low redshift matter density field as traced by galaxies [23, 63, 74]. MTs are particularly useful as they provide directional information that is not present in the scalar Minkowski functionals.

In this paper, we aim to investigate how various cosmological effects: non-linear gravitational evolution, redshift-space distortion (RSD), and the presence of massive neutrinos, alter the morphology of the excursion sets of the three-dimensional matter density field relative to its initial, Gaussian state. Each of these phenomena introduces characteristic modifications to the matter density field. Gravitational evolution drives mode coupling and enhances non-Gaussianity, RSD induces anisotropy in the observed density field through velocity-induced distortions along the line of sight, and free-streaming massive neutrinos damps small-scale power [75–77]. Each will imprint a characteristic signal on the morphology of excursion sets that we will quantify in what follows. We focus on scales $R_G \sim 10\,h^{-1}\,\mathrm{Mpc}$ throughout, which are simultaneously weakly non-Gaussian while also being poorly described by standard perturbation theory. These are precisely the scales that can be probed by the current generation of galaxy surveys.

A detailed analysis in [78] precisely quantified the impact of various systematic effects on the genus statistic of gravitationally evolved matter and dark matter halo density fields. The study considered finite pixel size, non-linear gravitational evolution, redshift-space distortion (RSD), shot noise due to finite sampling, and halo bias. In a similar study, analysis of the two-dimensional genus statistic of the galaxy distribution using Horizon Run 4 simulations [79] focused on similar systematic effects, finding that while pixel and gravitational effects are

JCAP08(2026)082

relatively minor ($\leq 1\%$), RSD and shot noise can induce genus amplitude changes up to $\sim 10\%$, though these can be mitigated by thick redshift shells and mass-based galaxy sampling [80]. Several studies have also explored, in a quantitative framework, the potential of leveraging the morphological properties of large-scale structure (LSS) to constrain the sum of neutrino masses, M_ν [47, 48, 81, 82]. These works utilize statistics such as Minkowski Functionals, power spectrum, bispectrum, marked statistics to capture the imprints of massive neutrinos (scale-dependent suppression of small-scale structure) in the morphology of matter density or galaxy density fields. They demonstrate that LSS morphology can serve as a complementary probe to traditional power spectrum-based methods in constraining M_ν and simultaneous measurement of both yields significant improvement over the power spectrum constraints.

The present analysis is focused on characterizing the deviations in morphology and topology induced by the above mentioned physical phenomena, rather than constraining cosmological parameters. To quantify these effects, we employ a set of statistical measures including Minkowski Functionals, Betti numbers, and Minkowski Tensors. This work is a purely numerical study based on the Quijote simulations [83], a large-scale suite of N-body simulations designed for cosmological inference using machine learning and statistical methods. The availability of thousands of realizations with controlled variations of cosmological parameters, including the neutrino mass, allows us to isolate the impact of each physical effect on the morphology of the matter distribution.

This paper is organized as follows. In section 2, we provide a brief overview of the Quijote simulation data used in our analysis and introduce the set of morphological statistics employed — namely, Minkowski Functionals, Minkowski Tensors, Betti numbers, as well as the averaged properties of individual connected components and holes. Section 3 focuses on the morphological properties of Gaussian random fields (GRFs), which represent the initial conditions of the Universe at some unspecified initial time. The impact of gravitational collapse, redshift space distortion, massive neutrinos, galaxy bias and shot noise on our statistics are presented in sections 4–8. We describe the response of our summary statistics to cosmological parameters in section 9 and summarize our results in section 10.

2 Data and methodology

We use dark matter simulations to study how various cosmological processes affect the morphology and topology of the matter density field. In this section we review the data used in our analysis and the summary statistics that we measure.

2.1 Data

We use the Quijote simulations for this study [83], which are an ensemble of cosmological scale dark matter simulations; $\sim 44,000$ realisations of 512^3 particles gravitationally evolved in $L = 1000\,h^{-1}\,\mathrm{Mpc}$ boxes from $z = 127$ to $z = 0$. Specifically, we use $N_{\rm real} = 50$ redshift zero snapshot boxes and construct real space density fields by binning the dark matter particles into a uniform 512^3 Cartesian grid of resolution $\Delta = 2\,h^{-1}\,\mathrm{Mpc}$. We then define the number density field $\delta_{\{i,j,k\}} = (n_{\{i,j,k\}} - \bar{n})/\bar{n}$, where $n_{\{i,j,k\}}$ is the number of particles in the $\{i, j, k\}$ pixel and $\bar{n}$ is the mean number of particles per pixel. Throughout this work, we refer to the particle number density field simply as the matter density field. We smooth this

JCAP08(2026)082

field in Fourier space using a Gaussian kernel $W(kR_{\rm G}) = e^{-k^2R_G^2/2}$. After smoothing, the field is again mean-subtracted and normalised to unit variance. We adopt the smoothing scale $R_{\rm G} = 10\,h^{-1}\,$Mpc throughout this work, which is the typical mean galaxy separation of current generation galaxy surveys.

The Quijote simulations are performed using a wide range of different cosmological parameter sets. We focus predominantly on the fiducial, Planck ΛCDM cosmology with parameters $\Omega_m = 0.3175$, $n_s = 0.9624$, $\Omega_b = 0.049$, $h = 0.6711$, $\sigma_8 = 0.834$, but also consider variations of cosmological parameters in section 9 and the inclusion of massive neutrinos in section 6. Details of how massive neutrinos were modelled in the Quijote simulations can be found in [84].

To compare our results to the initial condition of the matter density field, we generate $N_{\rm real} = 50$ realisations of a Gaussian random field with the same cosmological parameters as the fiducial Quijote simulations. The Gaussian fields are generated on a regular grid in Fourier space and inverse fast Fourier transformed using the same size and resolution as the Quijote snapshot boxes. They are finally smoothed with $R_{\rm G} = 10\,h^{-1}\,$Mpc, mean-subtracted and unit variance normalized exactly as the Quijote data, and the same statistics extracted.

The summary statistics are extracted from the fields using the numerical procedures described in [74], using a marching tetrahedron algorithm to generate iso-field surfaces. We direct the reader to appendices A and B of that work for further details.

2.2 Minkowski Functionals, Betti numbers, Minkowski Tensors

Given a mean-subtracted, smoothed dark matter density field $\delta(\mathbf{x})$ with variance $\sigma_0^2 = \langle\delta^2\rangle$, we define the excursion set at threshold ν as $Q(\nu) = \{\mathbf{x}\,|\,\delta(\mathbf{x}) \geq \nu\sigma_0\}$. The set $Q(\nu)$ contains all spatial regions where the density contrast exceeds a specified threshold. We denote its boundary by ∂Q. For a typical ν, Q is not one continuous region but rather consists of disjoint subsets or elements, Q_i, with non-intersecting boundaries ∂Q_i, where i indexes each element. Throughout this work we call each individual element as a *connected component*, following the mathematics nomenclature.[1] Similarly, we can construct excursion sets using all spatial points equal to or below the threshold, as, $\widetilde{Q}(\nu) = \{\mathbf{x}\,|\,\delta(\mathbf{x}) \leq \nu\sigma_0\}$. Akin to Q, $\widetilde{Q}$ is composed of disjoint elements $\widetilde{Q}_i$, with non-intersecting boundaries $\partial\widetilde{Q}_i$. We refer to each $\widetilde{Q}_i$ as a *cavity*, or interchangeably *hole*, since $\widetilde{Q}_i$'s are manifested as cavities inside connected components (see figure 2 of [85]). Both connected components and cavities can be either simply or multiply connected, and here we make no distinction regarding their topology. Both ∂Q_i and $\partial\widetilde{Q}_i$ are orientable surfaces, but they are distinguished by opposite sense of orientation.

By varying ν, one can probe the morphology of a given field across different threshold levels — from high-density peaks ($\nu \gg 0$) to deep minima ($\nu \ll 0$). In this paper, to characterize the geometric and topological properties of excursion sets, we employ two different families of morphological descriptors that can be classified as: (1) volume averaged statistics defined for the total excursion set Q, and, (2) local statistics that quantify the morphology of individual Q_i and $\widetilde{Q}_i$. The definitions for these two classes of statistics are given below.

[1] In the cosmology literature, the disjoint elements are also referred to as 'excursion regions'.

JCAP08(2026)082

2.2.1 Volume averaged statistics

Minkowski Functionals: The most widely adopted statistics in cosmology that utilize excursion sets are the Minkowski Functionals (MFs), which encode the morphology and topology of a field. In three dimensions we define the four MFs as

$$W_0 = \frac{1}{V}\int_Q dV\,, \quad W_1 = \frac{1}{6V}\int_{\partial Q} dA\,, \quad W_2 = \frac{1}{3\pi V}\int_{\partial Q} G_2 dA\,, \quad W_3 = \frac{1}{4\pi^2 V}\int_{\partial Q} G_3 dA\,, \tag{2.1}$$

where ∂Q is the boundary $\delta = \nu\sigma_0$, V is the total volume of the domain and $G_2 = (R_1^{-1} + R_2^{-1})/2$ and $G_3 = (R_1 R_2)^{-1}$, with R_1, R_2 being the principal curvatures of the surface ∂Q. These statistics respectively encode the volume enclosed, surface area, mean and Gaussian curvatures of the excursion set boundary. They are defined here as densities, and as such can be related to local one-point cumulants of the field under the assumption of statistical homogeneity.

Betti numbers: Among the MFs, W_3 is a purely topological quantity that is invariant under continuous deformations of the excursion sets. It can be expressed in terms of three Betti numbers, which further characterize the topology of these sets. Specifically, b_0 denotes the number of connected components Q_i of an excursion set, and b_2 the number of distinct cavities $\widetilde{Q}_i$. The third one, b_1, denotes the number of tunnels or loops which measure the degree of multiply-connectedness of Q_i and $\widetilde{Q}_i$. The alternating sum of the Betti numbers is then related to W_3 [11] via

$$W_3 \propto -b_0 + b_1 - b_2. \tag{2.2}$$

We direct the reader to [38, 43, 44] for a detailed description of these statistics and other related topological measures such as persistence diagrams.

Minkowski Tensors: These are tensorial generalizations of MFs that capture directional information. We consider two translation invariant, rank-2 MTs defined as

$$W_1^{0,2} = \frac{1}{6V}\int_{\partial Q} \hat{n}\otimes\hat{n} dA\,, \qquad W_2^{0,2} = \frac{1}{3\pi V}\int_{\partial Q} G_2\hat{n}\otimes\hat{n} dA \tag{2.3}$$

where $\hat{n}$ is the unit normal to ∂Q and $\otimes$ denotes the symmetric tensor product. For the purpose of the present study, these are 3×3 Cartesian tensors, although see [86] for a discussion of the plane parallel limit and radial redshift space distortions. For the coordinate system chosen in this work (Cartesian basis aligned with snapshot box axes), all information is contained in the diagonal elements of these matrices, which we denote as $W_1^{0,2}|_\mu{}^\mu$ and $W_2^{0,2}|_\mu{}^\mu$ with $\mu = 1, 2, 3$. In redshift space, rotating the coordinate system into misalignment with the line-of-sight would generate off-diagonal elements, but for real space, isotropic fields, both tensors are proportional to the identity matrix. We direct the reader to [7, 74] for a detailed definition of these quantities and associated numerical methodologies in three dimensions.

2.2.2 Morphology of individual connected components and cavities

We next focus on the morphology of individual connected components Q_i and cavities $\widetilde{Q}_i$, and define three summary statistics that quantify their average morphology. The first is the

JCAP08(2026)082

effective radius of connected components and cavities, which are given by:

$$R_{\rm eff}^{\rm con} = \frac{1}{b_0}\left(\frac{3}{4\pi}\right)^{1/3}\sum_{i=1}^{b_0}\left(\int_{Q_i} dV\right)^{1/3}, \tag{2.4}$$

$$R_{\rm eff}^{\rm cav} = \frac{1}{b_2}\left(\frac{3}{4\pi}\right)^{1/3}\sum_{i=1}^{b_2}\left(\int_{\widetilde{Q}_i} dV\right)^{1/3}. \tag{2.5}$$

These two statistics measure the typical sizes of individual elements by averaging over the sizes of all Q_i and $\widetilde{Q}_i$, respectively, as functions of threshold. An important property of these definitions is that the non-linear mapping

$$\int_{Q_i} dV \mapsto \left(\int_{Q_i} dV\right)^{1/3}, \tag{2.6}$$

does not commute with the sum over elements. This means that the random variables $R_{\rm eff}^{\rm con,\,cav}$ cannot be expressed purely in terms of the volume averaged quantities W_0, b_0 and b_2. We elaborate on the information content of these statistics in appendix B.

The remaining two statistics quantify the average shapes of individual Q_i and $\widetilde{Q}_i$. For connected components, we first compute Minkowski tensors for each Q_i,

$$W_{1,\,i}^{0,2} = \frac{1}{6}\int_{\partial Q_i}\hat{n}\otimes\hat{n}dA\,, \qquad W_{2,\,i}^{0,2} = \frac{1}{3\pi}\int_{\partial Q_i} G_2\hat{n}\otimes\hat{n}dA\,, \tag{2.7}$$

and their eigenvalues

$$\Lambda_{\mu,i}^{\rm con\,(1)}, \qquad \Lambda_{\mu,i}^{\rm con\,(2)}, \quad \mu = 1,2,3\,, \tag{2.8}$$

following the ordering $\Lambda_{1,i} \leq \Lambda_{2,i} \leq \Lambda_{3,i}$ such that $\Lambda_{3,i}$ corresponds to the longest principal axis. Dimensionless shape parameters are then defined as [66]

$$\beta_{J,i}^{\rm con\,(1)} = \frac{\Lambda_{J,i}^{\rm con\,(1)}}{\Lambda_{3,i}^{\rm con\,(1)}} \leq 1\,, \qquad \beta_{J,i}^{\rm con\,(2)} = \frac{\Lambda_{J,i}^{\rm con\,(2)}}{\Lambda_{3,i}^{\rm con\,(2)}} \leq 1\,, \quad J = 1,2 \tag{2.9}$$

These ratios are scale-invariant and measure only shape anisotropy. Spherical objects have $\beta = 1$, whereas small β indicates elongated structures.

Averaging over the shape parameters of all connected regions gives the summary statistics

$$\beta_J^{\rm con(1)} = \frac{1}{b_0}\sum_{i=1}^{b_0}\beta_{J,i}^{\rm con\,(1)}, \quad \beta_J^{\rm con\,(2)} = \frac{1}{b_0}\sum_{i=1}^{b_0}\beta_{J,i}^{\rm con\,(2)}. \tag{2.10}$$

For cavities, we can perform exactly the same calculation, arriving at the corresponding average shape parameters,

$$\beta_J^{\rm cav(1)} = \frac{1}{b_2}\sum_{i=1}^{b_2}\beta_{J,i}^{\rm cav\,(1)}, \quad \beta_J^{\rm cav\,(2)} = \frac{1}{b_2}\sum_{i=1}^{b_2}\beta_{J,i}^{\rm cav\,(2)}\,. \tag{2.11}$$

Similarly to the quantities $R_{\rm eff}^{\rm con,cav}$, shape parameters $\beta_J^{\rm con,cav\,(1,2)}$ are constructed by applying a non-linear transformation (tensor components $\rightarrow$ eigenvalues $\rightarrow$ ratios) to individual objects

JCAP08(2026)082

prior to averaging, and so cannot be expressed purely in terms of the volume-averaged statistics $W_1^{0,2}$, $W_2^{0,2}$, b_0, b_2.

Geometrically, the tensors $W_1^{0,2}$ and $W_2^{0,2}$ measure the overall anisotropy of all excursion sets in a globally defined coordinate system. In contrast, the shape parameters $\beta_J^{\mathrm{con,cav}\,(1,2)}$ are defined in a local coordinate system aligned with each object's principal axis, and the average is then performed over the corresponding number of objects. Thus, they provides a local measure of anisotropy of the field. In summary, we use the statistics $\left[W_0, W_1, W_2, W_3, b_0, b_2, W_1^{0,2}, W_2^{0,2}\right]$ to characterise the global morphology of the density field, and $\left[R_{\mathrm{eff}}^{\mathrm{con,cav}}, \beta_J^{\mathrm{con,cav}\,(1,2)}\right]$ to quantify the properties of individual connected components and cavities.

3 Morphology of excursion sets for GRF

We begin with the case of isotropic Gaussian random fields (GRFs) drawn from a ΛCDM power spectrum with the same cosmological parameters as the fiducial Quijote simulations. The morphological properties of these fields serve as a reference baseline, enabling us to isolate and quantify subsequent morphological deviations induced by cosmological processes such as gravitational collapse, redshift-space distortions, and the presence of massive neutrinos. All the statistics considered in this section are well studied in the literature, with the exception of the effective radius. For GRFs, analytic expressions for ensemble expectations of MFs [87] are given by,

$$W_k(\nu) = \frac{1}{(2\pi)^{\frac{k+1}{2}}} \frac{\omega_3}{\omega_{3-k}\omega_k} \left(\frac{\sigma_1}{\sqrt{3}\sigma_0}\right)^k e^{-\nu^2/2} H_{k-1}(\nu), \tag{3.1}$$

where $k = 0, 1, 2, 3$, $\sigma_1^2 = \langle|\nabla\delta|^2\rangle$, H_0, H_1, H_2 are probabilist Hermite polynomials, and $H_{-1} = \sqrt{\frac{\pi}{2}} e^{\frac{\nu^2}{2}} \mathrm{erfc}\left(\frac{\nu}{\sqrt{2}}\right)$. The ω_k constants are $\omega_0 = 1$, $\omega_1 = 2$, $\omega_2 = \pi$ and $\omega_3 = \frac{4\pi}{3}$. The corresponding functional forms for global MTs are proportional to the MFs. Apart from the MFs and MTs, closed-form expressions are not known for the other statistics measured in this work.

In the top row of figure 1, we present the ensemble averaged Minkowski Functional curves $W_{0,1,2,3}$ of excursion sets of the GRFs, together with their 1σ uncertainties. These curves follow the expected functional form given by eq. (3.1). Due to the $\delta \to -\delta$ invariance of the probability distribution of GRFs, the MFs exhibit the symmetries: $W_0(\nu) = 1 - W_0(-\nu)$, $W_1(\nu) = W_1(-\nu)$, $W_2(\nu) = -W_2(-\nu)$, $W_3(\nu) = W_3(-\nu)$. Furthermore, all cosmological information is encoded in the amplitude of these curves, which are only sensitive to the ratio $r_c = \sigma_0/\sigma_1$.

In the middle row of figure 1, we show the diagonal elements of the Minkowski Tensors $W_1^{0,2}$ (left panel), $W_2^{0,2}$ (middle panel), together with the three Betti numbers $b_{0,1,2}$ (right panel). The diagonal components of each MT are shown as solid cyan/yellow/pink lines, which overlap exactly in this case, while the off-diagonal elements (not shown) are consistent with zero. This behaviour reflects the statistical isotropy of the Gaussian field, for which $W_1^{0,2} \propto W_1\mathbb{I}$, $W_2^{0,2} \propto W_2\mathbb{I}$, where $\mathbb{I}$ is the identity matrix. This is in agreement with the results reported in [61], where the authors derive an analytic expression for the ensemble expectation

JCAP08(2026)082

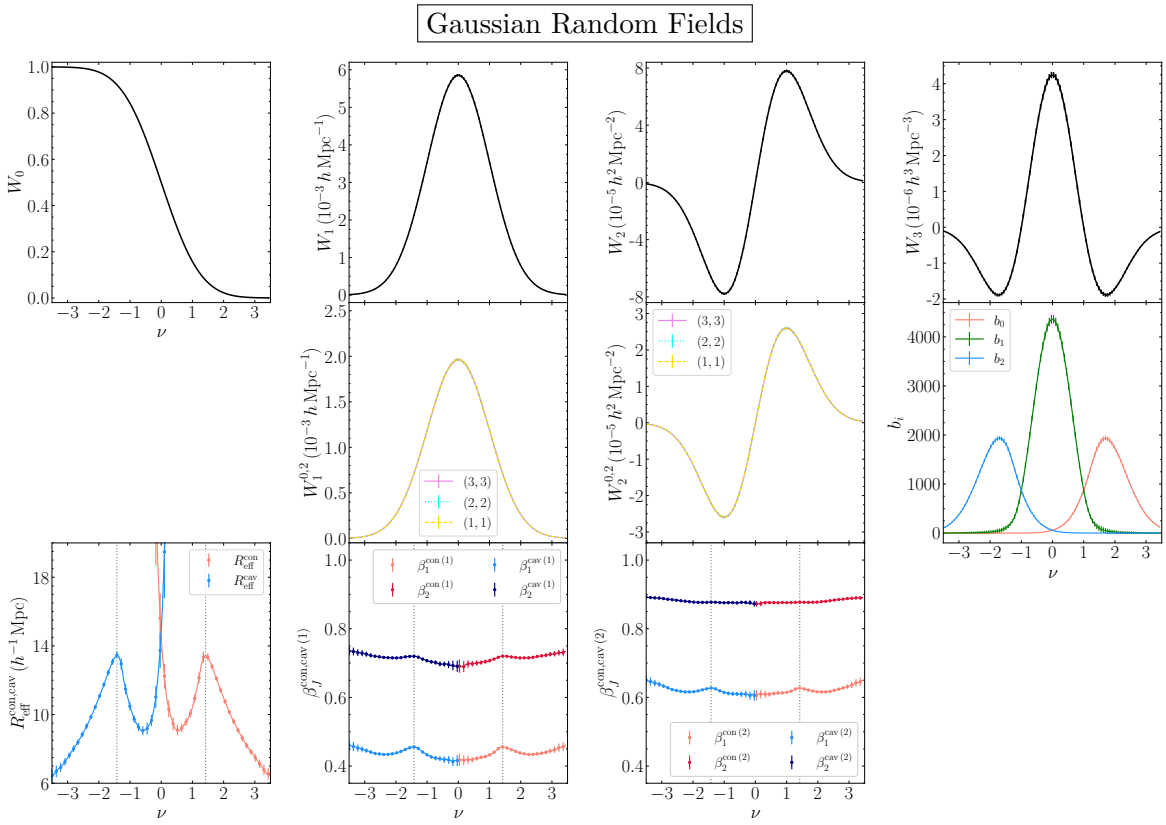


Figure 1. Morphological statistics measured from Gaussian random field realisations smoothed on a scale of $R_G = 10\,h^{-1}\,\mathrm{Mpc}$ with a Gaussian filter. *Top row*: The four Minkowski Functionals, shown by black curves with error bars indicating the 1σ scatter among realisations. *Middle row*: The two Minkowski Tensors $W_1^{0,2}$ (left) and $W_2^{0,2}$(middle), and the three Betti numbers (right). *Bottom row (left to right)*: Local statistics: the effective size ($R_{\mathrm{eff}}^{\mathrm{con,cav}}$), and the shape parameters ($\beta_J^{\mathrm{con,cav}\,(1)}$) and ($\beta_J^{\mathrm{con,cav}\,(2)}$). Connected components and cavities are shown in red and blue, respectively, while darker and lighter curves correspond to the two β eigenvalue ratios extracted from each Minkowski Tensor.

of $W_1^{0,2}$ for two-dimensional fields. They show that for an isotropic field, $W_1^{0,2} \propto W_1 \mathbb{I}$, which indicates that there is no additional information in MTs compared to MFs in the absence of any preferred direction.

The Betti numbers (second row, right panel) contain information that is not captured by the Minkowski Functionals [11, 14, 43–45, 85, 88–90]. At high thresholds, $\nu \gtrsim 2$, the genus is well approximated by $W_3 \simeq -b_0/V$ while for low thresholds, $\nu \lesssim -2$, one finds $W_3 \simeq -b_2/V$. In these regimes the topology of the excursion sets is relatively simple, being dominated by small isolated high-density peaks or low-density minima connected by saddle points. At intermediate thresholds $-2 \lesssim \nu \lesssim 2$, the topology becomes significantly more complex due to the presence of loops and embedded holes within larger connected regions. In this regime, the shape of the $b_{0,1,2}$ curves contain new information beyond the alternating sum $W_3 \sim (-b_0 + b_1 - b_2)/V$. Quantifying this statement is difficult, because closed-form expressions for ensemble averages of $b_{0,1,2}$ are not known. However, near $\nu \approx 0$, one has $W_3 \approx b_1/V$. Because each Betti number dominates at different threshold levels, [91, 92] introduced genus-related statistics — such as the cluster and void abundance parameters

JCAP08(2026)082

A_C and A_V, and the shift parameter $\Delta\nu$ — which summarize the information contained in b_0, b_2, and $b_1(\nu)$, respectively [11].

Unlike W_3, the Betti numbers cannot be written exactly in terms of local one-point cumulants of the field and its derivatives for any threshold, as they quantify the connectivity of critical points that lie above a given threshold. A previous study of Gaussian random fields has revealed that the shape of the Betti curves $b_{0,1,2}(\nu)$ is sensitive to the shape of the underlying power spectrum of the field [11]. This is in contrast to $W_3(\nu)$, for which the shape is exactly fixed by $W_3(\nu) \propto (1-\nu^2)\exp[-\nu^2/2]$, and only the amplitude is sensitive to the power spectrum.

In the bottom panels of figure 1, we show effective radii $R_{\rm eff}^{\rm con,cav}$ (left), and the shape parameters $\beta_J^{\rm con,cav(1)}$ (middle) and $\beta_J^{\rm con,cav(2)}$ (right). All three statistics exhibit distinctive maxima and minima as functions of ν, which reflect the changing morphology of the excursion sets. To describe this behaviour, we focus on $R_{\rm eff}^{\rm con}$ for the connected components (cf. red curve, bottom left panel). The interpretation for the cavities (blue curve) follows analogously under $\nu \to -\nu$.

At large thresholds $\nu \gtrsim 3$, the excursion set is dominated by isolated high-density peaks. As ν is lowered, two competing effects influence $R_{\rm eff}^{\rm con}$. First, existing objects grow in volume and merge as saddle points enter the excursion set, thereby increasing $R_{\rm eff}^{\rm con}$. Second, new and initially small isolated peaks appear, which has the effect of decreasing $R_{\rm eff}^{\rm con}$. In the range $\nu \gtrsim 2$, the first effect dominates, because the number of saddle points entering exceeds the number of new peaks (see the bottom left panel of figure 2 of [93]), leading to an overall increase of $R_{\rm eff}^{\rm con}$ with decreasing ν.

At $\nu \simeq 1.4$, $R_{\rm eff}^{\rm con}$ exhibits a distinct maximum. At this threshold, the largest excursion subsets amalgamate into a single structure, removing most of the large objects from the average and replacing them with a single contribution. Because $R_{\rm eff}^{\rm con}$ averages over the fractional power $V_i^{1/3}$, larger objects are effectively de-weighted and therefore do not dominate the average. This amalgamation reduces the mean while the more numerous small elements remain distinct. The effective radius therefore decreases until $\nu \sim 0.7$. Below this value, the percolating structure rapidly grows and dominates the excursion set, linking nearly all components. At this point, there is a second rapid turnaround in $R_{\rm eff}^{\rm con}$ and the statistic approaches the box size.

The $\beta_J^{\rm con,cav\,(1,2)}$ curves (bottom row, middle and right panels) encode the same morphological information as functions of threshold, but in terms of shape rather than size. The overall variation of the curves with ν is weaker than that of $R_{\rm eff}^{\rm con,cav}$. For example, in the middle panel we have $\beta_1^{\rm con\,(1)} \sim \beta_1^{\rm cav\,(1)} \sim 0.45$ and $\beta_2^{\rm con\,(1)} \sim \beta_2^{\rm cav\,(1)} \sim 0.75$, with only a $\sim 10\%$ variation across the full range of ν values considered. This indicates that the average connected components and cavities are well described as triaxial ellipsoids with nearly constant axis ratios. The increasing number of saddle points entering the excursion set causes $\beta_J^{\rm con\,(1,2)}$ to decrease slightly from high to intermediate thresholds, and the extrema at $\nu \simeq \pm 1.4$ coincide with the peak in $R_{\rm eff}^{\rm con,cav}$, arising from the same merging and percolating behaviour of the field. At low thresholds $|\nu| \lesssim 1.4$, the shape functions $\beta_J^{\rm con,cav\,(1,2)}$ are even less sensitive to the presence of the large percolating excursion set because the averages are performed over eigenvalue ratios, meaning that objects of all sizes are uniformly weighted in

JCAP08(2026)082

the average. For more information on the properties of the individual connected components and cavities, we direct the reader to appendices B and C.

In summary, the Minkowski Functionals (cf. top panels) probe the joint PDF of the field and its first and second derivatives, while the Minkowski tensors (second row, first two panels) probe the directional dependence. The Betti numbers (second row, right panel) contain information at threshold ranges $-2 \lesssim \nu \lesssim 2$ that is not fully captured by MFs and MTs. The average size and shape properties of connected components and cavities (bottom panels) characterize the percolation of the excursion sets as a function of threshold, providing a complementary perspective on the connectivity and large-scale organization of the field.

4 Gravitational evolution

In this section, we explore the impact of gravitational evolution on the morphology of excursion sets by comparing the non-linear matter density field at redshift $z = 0$ with the corresponding GRFs. We smooth the field on the relatively large scale $R_G = 10\,h^{-1}\,\mathrm{Mpc}$. Note that at this scale we are not probing non-linear structures such as clusters or voids as conventionally defined in the literature. Those objects are defined via at least one shell crossing event, indicating collapse along one or more dimensions. Our large-scale, isotropic smoothing kernel ensures that we remain in the single-stream, weakly non-Gaussian regime. At the same time, standard perturbation theory and the Edgeworth expansion of the field PDF are known to perform poorly for $R_G \lesssim 10\,h^{-1}\,\mathrm{Mpc}$ (see e.g. figure 4 of [94]). Our choice of R_G is deliberately selected to probe an intermediate regime: below the scales that can be accurately described by perturbation theory, yet sufficiently large that the field remains single-stream.

The first point to note is that the overwhelmingly dominant effect of gravitational evolution on the one-point statistics of the density field is to skew the PDF towards high positive values. This arises due to odd cumulants $\langle \delta^n \rangle$, starting with the bispectrum $n = 3$, being induced via non-linear mode coupling. To illustrate this effect, in figure 2, we present the same statistics as in the previous section, now for the $z = 0$ dark matter snapshots. The colour scheme for all panels is the same as in figure 1. For comparison, in every panel we also exhibit the Gaussian random field measurements from the previous section as grey filled bands. The positive skewness of the evolved field is clearly the most dominant feature of the coloured curves.

Figure 2 presents a direct comparison between Gaussian and non-Gaussian fields at equal iso-field thresholds ν. Although this comparison is well defined, it is not the most suitable choice for understanding the effect of gravity as manifested in the morphological statistics. The reason is that since gravitational evolution strongly skews the PDF of the density field, $P(\delta)$, a fixed threshold ν corresponds to different quantiles of the Gaussian and non-Gaussian PDFs. In other words, for the same value of ν, the two excursion sets of the Gaussian and gravitationally evolved density field sample different regions of the underlying PDFs.

One way to overcome the issue of quantile mismatch and to meaningfully compare the morphology of Gaussian and non-Gaussian fields is to express morphological statistics as functions of the volume threshold ν_v defined by [95–97]:

$$f_v = \frac{1}{\sqrt{2\pi}} \int_{\nu_v}^{\infty} e^{-t^2/2} dt, \tag{4.1}$$

JCAP08(2026)082

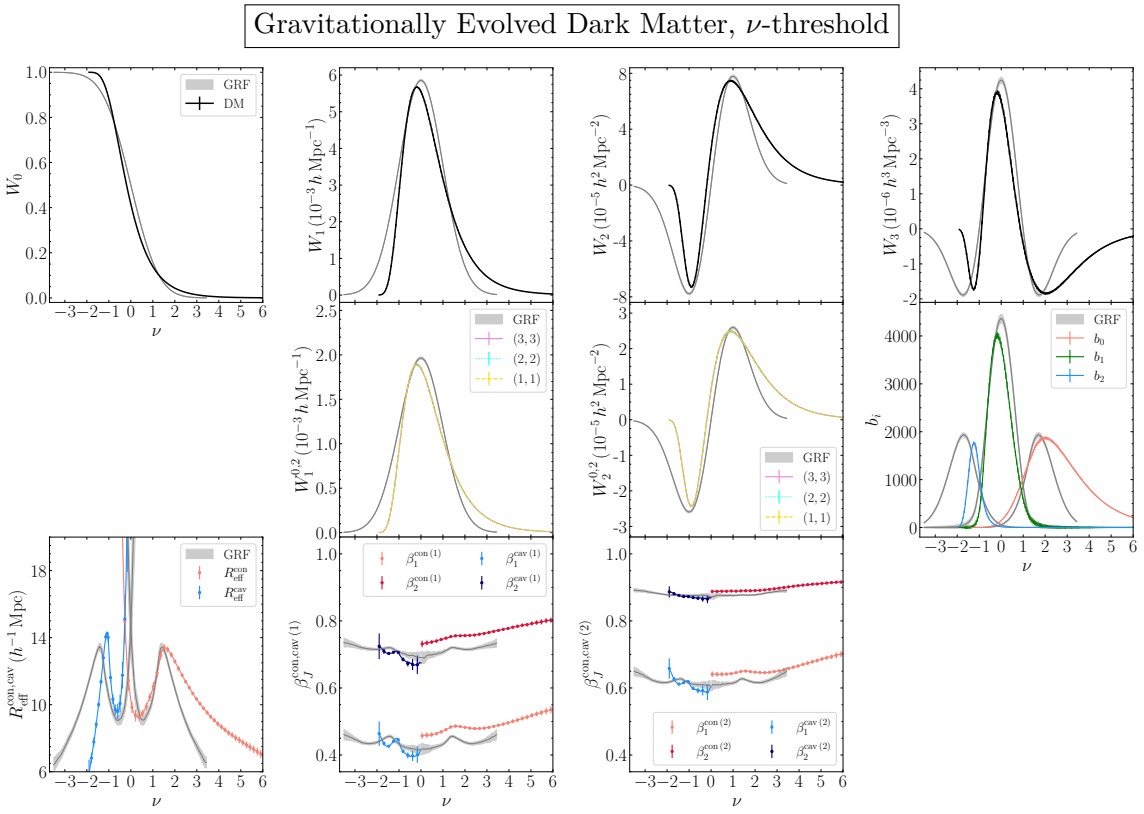


Figure 2. Morphological statistics measured for gravitationally evolved dark matter fields as a function of iso-field threshold ν. Coloured curves show the dark matter results, while the grey curves correspond to the Gaussian case from figure 1 and are included for comparison. The panel layout and colour scheme follow figure 1.

where f_v is the fractional volume of the field above ν_v [95]. For each given field, we fix a value of f_v and use it to determine ν_v (the mapping is one-to-one). We then consider the morphological statistics as functions of ν_v. A demonstration of this mapping is shown in figure 10 in appendix A. For a Gaussian field, f_v is exactly W_0, and ν_v is identical to ν. However, for a gravitationally evolved non-Gaussian field, $\nu_v \neq \nu$ (see figure 10 for their exact relation). Therefore, comparing excursion sets of the Gaussian and non-Gaussian fields by fixing ν_v corresponds to comparing the two fields at the same volume fraction, or equivalently at the same quantile of the field distribution. Using ν_v exactly transforms the one-point PDF of the field δ to its Gaussian form.

The impact of using the volume threshold can be understood as follows. The volume fraction of the excursion set gives the cumulative one-point probability of the field, assuming ergodicity. Hence only $P(\delta)$ is required to determine its statistical properties. In contrast, other morphological statistics (higher order MFs, Betti numbers and associated local statistics) are determined not just by $P(\delta)$, but by the joint PDF of δ and its higher derivatives. Note that the derivative of the field along the i^{th} coordinate can be written as

$$\partial_i \delta = \lim_{\epsilon \to 0} \frac{1}{\epsilon} \left[\delta(x_i + \epsilon) - \delta(x_i)\right], \tag{4.2}$$

JCAP08(2026)082

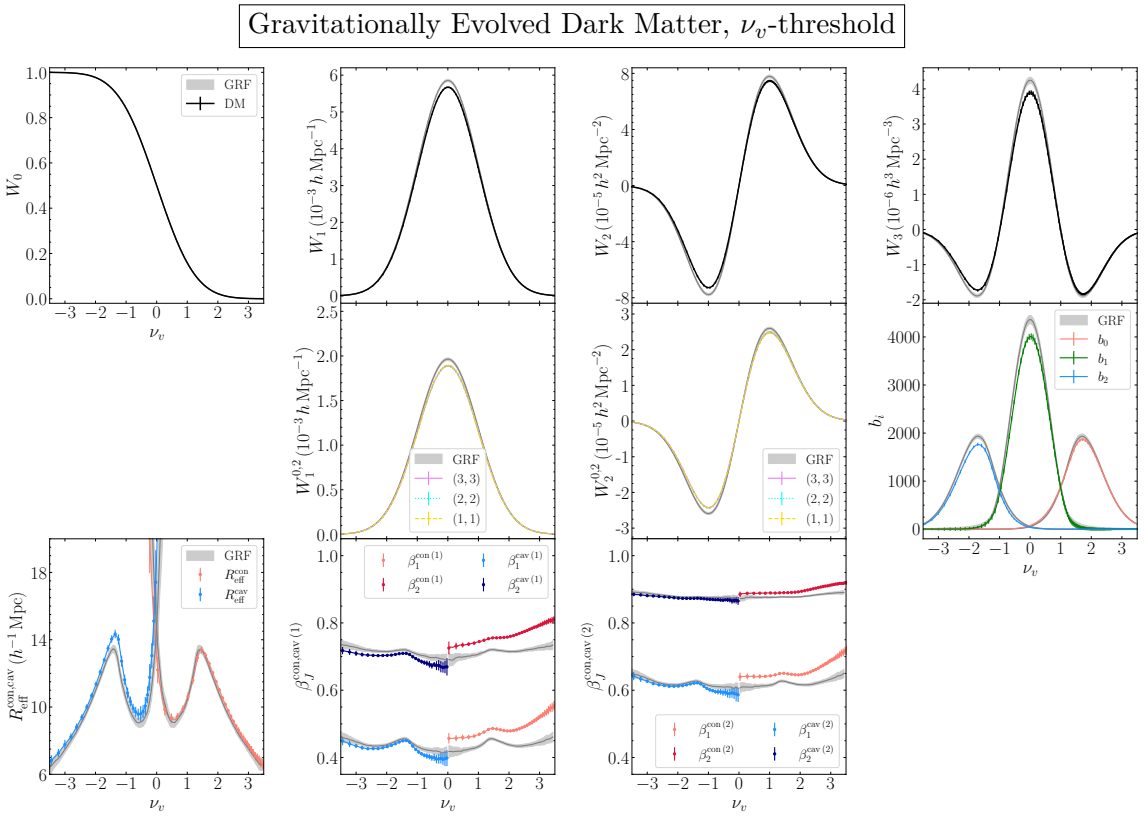


Figure 3. Identical to figure 2, except that the coloured dark matter curves are presented as functions of volume threshold ν_v as opposed to conventional iso-field values ν. The grey Gaussian reference curves are unaffected by the $\nu \to \nu_v$ transformation.

so that all correlations between the field at x_i and $x_i + \epsilon$, whose ensemble average is not zero in the limit $\epsilon \to 0$, are encoded in the derivatives of the field. Using the volume threshold then amounts to removing the purely local, one-point contribution to the non-Gaussianity, while retaining all the 'non-local' information contained in the joint PDF of the field and its derivatives. Since we wish to isolate the impact of gravitational evolution on the spatial correlations of the field, we present our measurements of morphological statistics of the dark matter fields, as functions of ν_v, in figure 3. The colour scheme matches that of figure 2.

In the first row of figure 3, we compare the Minkowski functional curves computed from the gravitationally evolved non-linear matter density field and those from an initial GRF (shown as black and grey curves, respectively). For the W_1, W_2, and W_3 curves, we observe a noticeable suppression of the amplitudes in the dark matter measurements. This is the well-known *gravitational smoothing* effect [78, 97], which can be described using the four-point function on quasi-linear scales [94]. There is also some residual skewness in the curves, which is most apparent in W_3, with negative thresholds more significantly impacted by the gravitational evolution.

Although non-linear gravitational evolution introduces significant non-Gaussianity, it preserves statistical isotropy. This property is verified by the globally averaged Minkowski Tensors $W_1^{0,2}$ and $W_2^{0,2}$, shown in the middle panels of figure 3. The diagonal components of

JCAP08(2026)082

these rank-2 tensors, $W_1^{0,2}|^{\mu}_{\mu}$ and $W_2^{0,2}|^{\mu}_{\mu}$ (where $\mu = 1, 2, 3$), overlap exactly for the non-linear matter field, while the off-diagonal elements (not shown) remain consistent with zero. Locally, we expect gravitational collapse to occur anisotropically, with matter collapsing onto wall saddle points from underdense regions, finally fed into peaks via filaments. However, there is no preferred global orientation in these locally anisotropic processes, and the MTs are constructed in a coordinate system defined over the entire domain. Provided the spatial averaging is performed over volumes much larger than the characteristic scale of individual structures, gravitational collapse preserves statistical isotropy as quantified by the Minkowski tensors.

The remaining four panels of the figure 3: the Betti curves (second row, right panel) and the individual structure morphology (bottom-row panels) illustrate how gravitational collapse affects the connected components and cavities. The blue curves inform us that in the $z = 0$ dark matter field there are fewer but larger cavities compared to the Gaussian reference. The change in number and size of cavities is likely due to the merging of minima critical points through the consumption of wall saddles. In contrast, b_0 (red curve) informs us that there are slightly fewer connected components, but their size $R_{\rm eff}^{\rm con}$ remains indistinguishable from that in the Gaussian field. The decrease in b_2 is significantly larger than b_0, which indicates that minima-wall saddle merging is a more efficient process than peak-filament merging on these large scales.

The shape of the cavities, characterized by $\beta_J^{{\rm cav}\,(1,2)}$ (blue curves, bottom-row middle and right panels) is marginally less spherical than the Gaussian counterparts, but otherwise practically unchanged. The shape of the connected components (red curves) evolve more significantly, becoming more spherical for all thresholds probed. The degree of sphericalization increases with increasing ν_v. We also note that the peaks of the curves in the bottom panels remain located at $\nu_v \simeq 1.4$, unaffected by the gravitational evolution after the $\nu \to \nu_v$ threshold re-mapping.

The overall effect of gravitational collapse on these quasi-linear scales is to merge a fraction of minima via the consumption of wall saddle points, thereby increasing their average size, while simultaneously making the peaks more spherical. The Minkowski Functionals and tensors exhibit reduced amplitudes and a slight skewness relative to the Gaussian case.

5 Redshift space distortion

Next, we consider the effect of redshift-space distortion (RSD) on excursion-set morphology. This phenomenon corresponds to the anisotropic deformation of observed structures caused by contamination of cosmological redshifts by line-of-sight peculiar velocities. The physical anisotropic effects of RSD can be understood as two distinct phenomena. The first is the 'Kaiser effect' in which coherent peculiar velocities cause large-scale structures to appear compressed along the line of sight [98, 99]. This gravitational infall is observed on all scales. The second is the 'Finger-of-God effect' [100] on smaller scales due to large random velocities of virialised objects which stretch structures along the line of sight, producing elongations pointing toward the observer.

Under the plane-parallel approximation, redshift-space density field, $\delta(\mathbf{s})$, can be generated from the real-space density field by perturbing particle positions $\mathbf{x}$ along the line-of-sight direction. If the line of sight is taken to be the x_3-axis (the $\mathbf{e}_3$ direction), the displacement

JCAP08(2026)082

is determined by the particle peculiar velocity $\mathbf{v}$ such that:

$$\mathbf{s} = \mathbf{x} + \mathbf{e}_3(\mathbf{v}.\mathbf{e}_3)\frac{1+z}{H(z)}. \tag{5.1}$$

Because RSD explicitly breaks statistical isotropy, we expect shapes and sizes of excursion sets to differ between directions parallel and perpendicular to the line of sight. In this section, we investigate these anisotropic effects.

5.1 Linear RSD

Before we study the full, non-linear effect of redshift-space distortion on the evolved $z = 0$ dark matter particle distribution, we first consider the linear regime. We generate linear redshift-space distorted fields by taking the isotropic Gaussian random fields $\delta^{(r)}(\mathbf{x})$ constructed in section 3 and applying the following transformation in Fourier space [98]:

$$\delta^{(s)}(\mathbf{k}) = (1 + f\mu^2)\delta^{(r)}(\mathbf{k}) \tag{5.2}$$

where $\mu = \mathbf{e}_3.\mathbf{k}/|\mathbf{k}|$ and $f = \Omega_m^\gamma$ with $\gamma \simeq 0.55$. The superscripts (r) and (s) denote real and redshift space, respectively. After performing the inverse Fourier transform, the resulting field contains the anisotropic Kaiser signal but does not include the non-linear Finger-of-God contribution or higher-order anisotropic mode couplings. Because the mapping between real- and redshift-space fields is linear, and the RSD operator is deterministic, the field $\delta^{(s)}(\mathbf{x})$ remains Gaussian.

We generate $N_{\rm real} = 50$ anisotropic Gaussian random fields using the Quijote fiducial cosmology and a smoothing scale $R_G = 10\,h^{-1}\,$Mpc, and extract the global and local summary statistics, which are presented in figure 4. The color scheme matches that of figure 3. In each panel, the grey filled lines/bands represent the mean and uncertainty of the same statistics extracted from the corresponding real-space Gaussian fields.

In the top panels of figure 4, we see that Minkowski Functionals of the redshift-space fields (black curves) are practically indistinguishable from the corresponding real-space grey curves, with only a very small ($\sim 1\%$) decrease in their amplitudes in redshift space. The largest amplitude difference occurs for W_3, which has been calculated analytically in [101]. In the right panel of the second row, we present the Betti numbers, whose amplitudes are all marginally lower in redshift space, commensurate with W_3, in redshift space. In the sub-panel directly beneath, we present the difference between the redshift- and real-space Betti numbers together with the error on the mean of the measurement. The suppression is approximately 2%.

In the second row of figure 4, the middle panels display the Minkowski tensor components. We plot the components of $W_1^{0,2}$ and $W_2^{0,2}$, as well as the differences $\Delta W_i^{0,2} = W_i^{0,2}(\text{redshift}) - W_i^{0,2}(\text{real})$ for each principal axis $(1,1),(2,2),(3,3)$. The pink dashed curve corresponds to the tensor component oriented parallel to the line-of-sight, while the yellow and cyan curves are the two degenerate components perpendicular to the line-of-sight. The parallel and perpendicular components deviate significantly, demonstrating that the MTs capture the strong anisotropy imprinted by RSD on the matter density field. For the Gaussian fields considered in this subsection, this difference corresponds to a constant amplitude offset. In contrast to the scalar MFs, we find that MT components clearly capture the global anisotropy introduced by linear redshift-space distortions.

JCAP08(2026)082

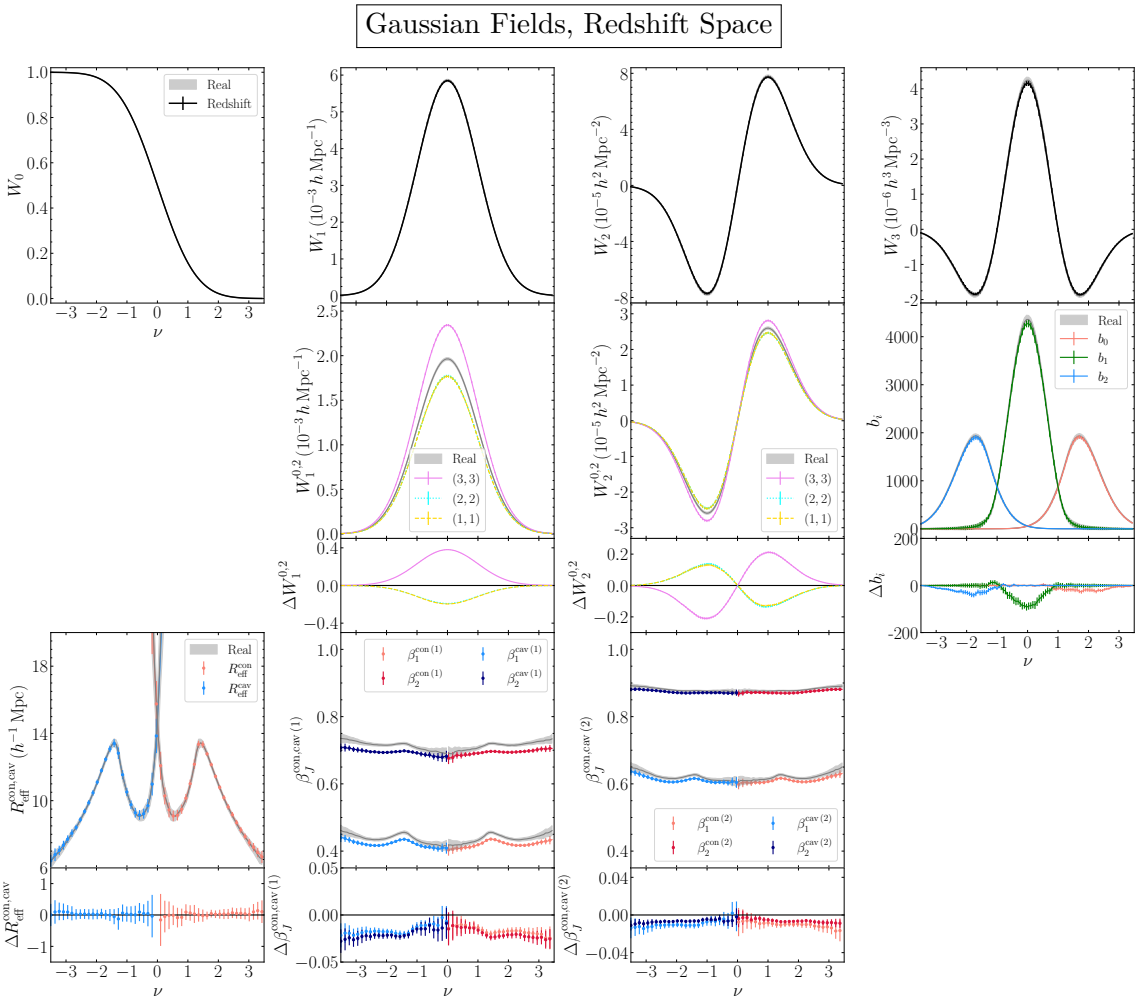


Figure 4. Morphological statistics measured for Gaussian fields in linear redshift space. Coloured curves show the redshift-space results, while the grey curves correspond to the isotropic Gaussian case from figure 1 and are included for comparison. The panel layout and colour scheme follow figure 1, except that the second and third rows include additional sub-panels showing the difference between the redshift- and real-space statistics.

In the third row (left panel), we find that the effective radii $R_{\mathrm{eff}}^{\mathrm{con,cav}}$ of connected components and cavities are practically unaffected by the linear redshift-space distortion operator. However, their shapes (middle and right panels) become systematically less spherical, i.e. more anisotropic, at all thresholds. In the lower sub-panels we present the difference between redshift- and real-space statistics. While the radii exhibit no measurable change, we observe decrease of ~ 0.03 and ~ 0.01 in $\beta_J^{\mathrm{con,cav}\,(1)}$ and $\beta_J^{\mathrm{con,cav}\,(2)}$, respectively. These values indicate that $\beta_J^{\mathrm{con,cav},(1)}$ responds more strongly to linear RSD than $\beta_J^{\mathrm{con,cav},(2)}$, implying that the presence of the mean curvature in the integrand of $W_2^{0,2}$ reduces its sensitivity to anisotropy compared to $W_1^{0,2}$.

In conclusion, while individual objects in real space are randomly oriented with respect to the line-of-sight $\mathbf{e}_3$, in redshift space their major axes have a tendency to be preferentially aligned with $\mathbf{e}_3$. The distortion effect is small but coherent, and is responsible for the systematic decrease in $\beta_J^{\mathrm{con,cav}\,(1)}$ and $\beta_J^{\mathrm{con,cav}\,(2)}$.

JCAP08(2026)082

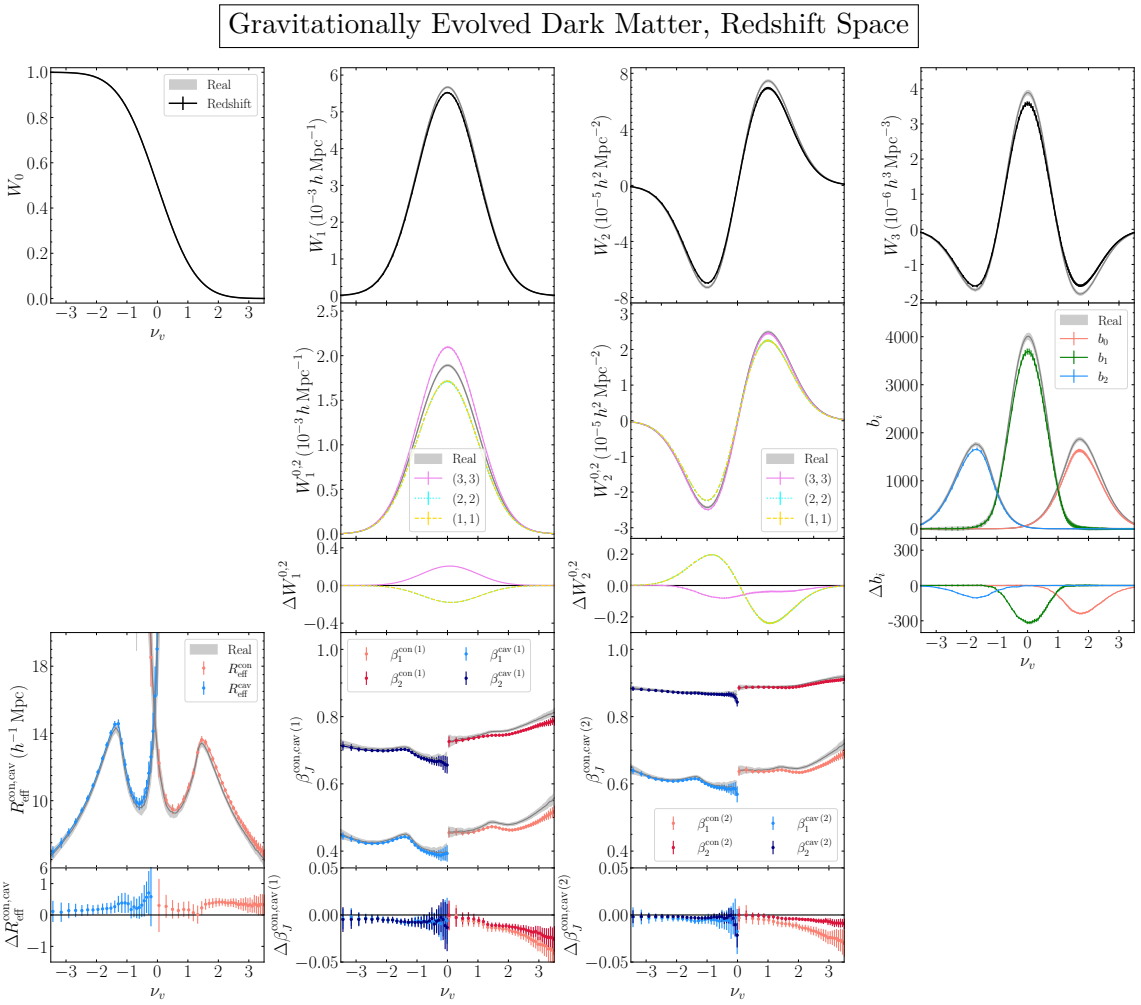


Figure 5. Morphological statistics measured for dark matter fields in non-linear redshift space. Coloured curves show the redshift-space results, while the grey curves correspond to real space dark matter from figure 3 and are included for comparison. The panel layout and colour scheme follow figure 4, including the sub-panels showing the difference between redshift and real space statistics.

5.2 Non-linear RSD

When we directly correct dark matter particle positions using their peculiar velocity along the line of sight, and use the new positions to construct a density field in redshift space, we are accounting for the full non-linear redshift-space distortion. This includes the higher order non-Gaussianty from the Kaiser effect as well as the non-linear Finger-of-God (FoG) stochastic velocity dispersion. Figure 5 compares the morphological statistics of the non-linear dark matter field in real space (grey curves) and redshift space (coloured curves). The colour scheme is the same as in previous figures.

In the top row, we find that compared to linear RSD summarized in the previous subsection, there is a larger decrease in amplitude of the MFs in redshift space compared to real space. This stronger suppression is due to the FoG dispersion along the line of sight, which washes out small-scale structures by acting as an additional source of anisotropic smoothing.

JCAP08(2026)082

Furthermore, it generates negative skewness, most clearly observed as asymmetry of W_3 (right panel). FoG affects overdense structures, leaving a larger imprint on $\nu_v > 0$ thresholds. This behaviour is also reflected in the Betti curves (second row, third panel), where the amplitude of b_0 (red curve) decreases more strongly compared to b_2. The processes of gravitational evolution and non-linear RSD act contrarily on the MFs in the following sense — the former primarily decreases the number of minima via merging, while the latter merges peaks along the line of sight via FoG smoothing. This makes the redshift-space statistics less skewed than their real-space counterparts. However, the two effects do not cancel one another, because both also reduce the overall amplitude of the Minkowski Functionals and Betti numbers.

The Minkowski Tensors (second row, first two panels) still contain the Kaiser signal, but the line-of-sight components are modified due to FoG. The yellow and cyan curves, representing the components perpendicular to the line of sight, present almost the same signal as their linear RSD counterparts in figure 4, specifically a constant amplitude decrease in redshift space. Contrarily, the line-of-sight-parallel curves (pink) are strongly modified in both amplitude and shape by non-linear effects [102]. In particular, the amplitude of the $(3,3)$ component of $W_1^{0,2}$ is reduced compared to the linear RSD signal, and for $W_2^{0,2}$ the shape of the $(3,3)$ curve is also modified. This is most clearly seen in the difference sub-panels, which again show $\Delta W_i^{0,2} = W_i^{0,2}(\text{redshift}) - W_i^{0,2}(\text{real})$, but now for the non-Gaussian fields.

We also consider how non-linear RSD influences the size and shape of individual structures. In the third row, left panel of figure 5, we present $R_{\text{eff}}^{\text{con}}$ for connected components (red curves) and $R_{\text{eff}}^{\text{cav}}$ for cavities (blue curves). In the sub-panel below, we show the differences $\Delta R_{\text{eff}}^{\text{con,cav}} = R_{\text{eff}}^{\text{con,cav}}(\text{redshift}) - R_{\text{eff}}^{\text{con,cav}}(\text{real})$. The overall effect is a small increase in effective radius, that is only significant in $R_{\text{eff}}^{\text{con}}$ at relatively high thresholds $\nu_v > 1.5$.

The lower middle and right panels of figure 5 show the shape anisotropy parameters $\beta_J^{\text{con,cav}(1)}$ and $\beta_J^{\text{con,cav}(2)}$. For the linear redshift-space distorted fields discussed in the previous section, both connected components and cavities exhibited lower values of $\beta_J^{\text{con,cav}(1)}$ and $\beta_J^{\text{con,cav}(2)}$ compared to their real-space counterparts. In contrast, distortions arising from non-linear RSD shift the average shape of cavities (blue curves) closer to their isotropic values, whilst increasing the ellipticity of high-threshold connected components (red curves). This trend can be understood physically: virialised motions within overdense regions generate strong FoG elongations along the line of sight, whereas underdense regions are less affected by such stochastic velocities. Once again, the effects of gravitational evolution and non-linear RSD act contrarily on the statistics: gravity slightly sphericalizes the connected components, while RSD elongates them. The two competing effects are not degenerate in the $\beta_J^{\text{con,cav}\,(1)}$ and $\beta_J^{\text{con,cav}\,(2)}$ curves, with redshift-space distortions inducing a smaller overall impact.

In summary, among the various phenomena studied in this work, RSD induces the most pronounced morphological changes in the Minkowski Tensors $W_1^{0,2}$ and $W_2^{0,2}$, and both linear and non-linear processes can be studied through their behaviour. Both gravitational evolution and RSD act to decrease the amplitude of the scalar MFs, while the two processes skew the MF curves in opposite directions. The shape of connected components, as quantified by $\beta_J^{\text{con}\,(1)}$, are most significantly altered by non-linear RSD effects, producing a threshold-dependent elongation of the excursion sets that is largest for isolated high-density peaks.

JCAP08(2026)082

6 Neutrino mass

Next, we consider the impact of massive neutrinos on excursion-set morphology by comparing simulations with and without a massive neutrino component (specifically $M_\nu = 0.4\,\mathrm{eV}$ vs. $M_\nu = 0$). We direct the reader to [83] for details on the implementation of massive neutrinos within the simulations, and [47, 48, 103] for a detailed study of the impact of neutrino mass on the Minkowski Functionals. When massive neutrinos are present as an additional energy component, there is an ambiguity in the definition of the dark matter field, specifically whether the massive neutrino particles are included in the definition of $\delta(\mathbf{x})$. In this work, density fields are constructed from dark matter particles only, excluding the neutrinos, since galaxy catalogues are expected to trace the clustered dark matter component. The mass value $M_\nu = 0.4\,\mathrm{eV}$ used in this work lies close to the current model-independent upper bound on the effective electron-flavour neutrino mass from the KATRIN experiment, $m_\beta < 0.45\,\mathrm{eV}$ at 90% confidence level [104]. When expressed in terms of the total neutrino mass, current cosmological analyses yield upper limits in the range $\Sigma m_\nu \lesssim 0.07$–$0.12\,\mathrm{eV}$ (95% C.L.), with the precise bound depending on the combination of datasets employed. The strongest constraints arise from analyses that include the latest baryon acoustic oscillation (BAO) data from the Dark Energy Spectroscopic Instrument (DESI), which substantially enhance sensitivity to neutrino mass [105, 106].

In figure 6, we present plots of our suite of summary statistics extracted from $N_{\mathrm{real}} = 50$, $M_\nu = 0.4\,\mathrm{eV}$ snapshot boxes at $z = 0$ (coloured curves) and the corresponding dark matter snapshot boxes with $M_\nu = 0$ (grey curves). The comparison is made in real space in order to disentangle the effects of RSD and massive neutrinos.

We first note that in all panels the impact of massive neutrinos is small and barely discernable by eye. In fact, the only effect is a slight decrease of the amplitudes of the MFs $W_{1,2,3}$, MTs $W_1^{0,2}$, $W_2^{0,2}$ and the Betti numbers. The amplitude drop is approximately $\sim$1–3%, and is largest for W_3 and the Betti numbers. This arises from the well-known damping of small-scale structures by neutrino free-streaming: because massive neutrinos fail to cluster efficiently below their free-streaming scale, they smoothen the high-contrast in the density field, reducing both the curvature and the total surface area of excursion-set boundaries. Although the damping effect is most pronounced on small scales $\lesssim 1\,h^{-1}\,\mathrm{Mpc}$, there is a small reduction in clustering at $\sim 10\,h^{-1}\,\mathrm{Mpc}$, as we see here. The effect is isotropic, as expected, and evidenced by the MTs remaining proportional to the identity matrix.

Further, massive neutrinos do not significantly modify the shape or size of individual components. The effective radius curves $R_{\mathrm{eff}}^{\mathrm{con,cav}}$ and the shape parameters $\beta_J^{\mathrm{con,cav}\,(1),(2)}$ for $M_\nu = 0.4\,\mathrm{eV}$ and $M_\nu = 0$ remain within the error on the mean of our measurements (figure 6, bottom panels). The shape parameters, $\beta_J^{\mathrm{con,cav}\,(1)}$ and $\beta_J^{\mathrm{con,cav}\,(2)}$, are nearly identical in the massive- and massless-neutrino case. This is expected as neutrino free-streaming damps fluctuations isotropically, reducing small-scale contrast without introducing any directional distortion, and thereby leaving the shape parameters essentially unchanged ($\Delta\beta_J^{\mathrm{con,cav}\,(1),(2)} \sim 0$).

The imprint of neutrinos on large-scale structures is subtle, and is predominantly observed on small scales. When extracting the Minkowski functionals from galaxy surveys, it is common to smooth the point distribution with a constant comoving scale to construct a continuous

JCAP08(2026)082

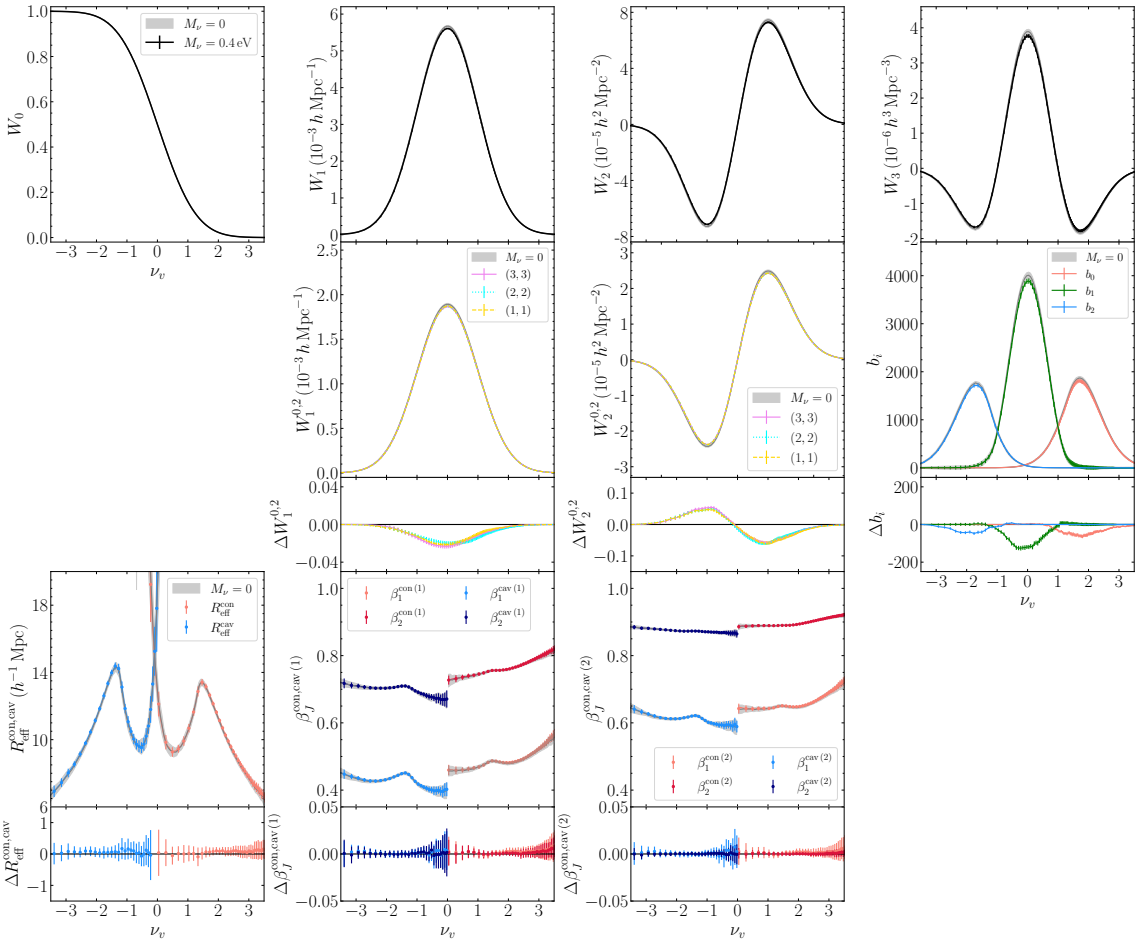


Figure 6. Morphological statistics measured for dark matter fields in real space including a massive neutrino component. Coloured curves show the massive-neutrino case, while the grey curves correspond to the massless-neutrino results from figure 3 and are included for comparison. The panel layout and colour scheme follow figure 5, including subpanels that show the difference between the massive- and massless-neutrino cases.

density field.[2] To minimize shot noise, a smoothing scale of $R_{\mathrm{G}} \sim \bar{r} = \bar{n}^{-1/3}$ is required, where $\bar{n}$ is the number density of the points. This requirement restricts us to large scales, as current generations of galaxy catalogues typically have $\bar{r} \simeq 10\,h^{-1}\,\mathrm{Mpc}$. To explore the effect of neutrinos, we will likely have to introduce alternative approaches, such as adaptive smoothing scales that preserve small-scale information.

7 Galaxy bias

We assess the impact of galaxy bias by comparing our fiducial dark matter distribution against galaxy fields constructed from the Molino mock catalog suite [109]. Built upon the Quijote

[2]However, topology can be extracted directly from point distributions without generating a continuous field [41, 107, 108].

JCAP08(2026)082

N-body simulations via a standard Halo Occupation Distribution (HOD) framework [110], the fiducial Molino catalogs feature a total volume of $(1\,h^{-1}\,\mathrm{Gpc})^3$ and a mean galaxy number density of $\bar{n}_g \sim 1.63 \times 10^{-4}\,h^3\,\mathrm{Mpc}^{-3}$. Because the mean particle separation is now larger, $\bar{r} = \bar{n}_g^{-1/3} \simeq 18\,h^{-1}\,\mathrm{Mpc}$, we smooth both the Molino and dark matter fields with smoothing scale $R_G = 20\,h^{-1}\,\mathrm{Mpc}$. We again use $N_{\mathrm{real}} = 50$ realisations of the fiducial Molino and dark matter snapshot boxes at $z = 0$.

As shown in figure 7, the scalar MFs of the Molino galaxy field (black curves) broadly trace the MFs of dark-matter baseline (grey curves), indicating that the overall morphology of the cosmic web is preserved by the biased tracer population. However, some systematic differences are visible in the shape of the MFs, with the largest effect in W_3. Specifically, W_1 is only marginally changed, W_2 is asymmetrically shifted with a higher peak amplitude and smaller trough, and W_3 is the most significantly skewed. These effects indicate that Minkowski functionals of the mock galaxy catalogues have a larger non-Gaussian component compared to the dark matter fields. The statistics W_1, W_2, W_3 are sensitive to successively more non-Gaussian cumulants, which explains why the non-Gaussianity is successively more visible from the top left to top right panels of the figure.

The most prominent signature of non-linear bias appears in W_3: on the negative threshold side ($\nu_v < 0$), the Molino curve sits above the dark matter baseline, whereas on the positive threshold side ($\nu_v > 0$), the black curve trough dips below the grey curve. This asymmetry in W_3 occurs because galaxy assembly is highly efficient within massive dark matter halos but suppressed in diffuse underdense environments, creating a skewed, non-linear mapping of the underlying matter distribution. Physically, deeper trough in W_3 at $\nu_v > 0$ indicates that galaxy distribution acts as a high-contrast tracer for the underlying cosmic web; by preferentially populating the high-density peaks (most massive dark matter halos), galaxies maps a more sharply defined and highly interconnected network of nodes and filaments than the smoother dark matter density field.

The non-Gaussianity is further observed in the Betti number curves, shown in the middle row, right panel. The Molino galaxy field shows an enhanced abundance of connected components, (b_0), relative to the dark-matter field, while the number of cavities, (b_2), is reduced. The shape parameters ($\beta_J^{\mathrm{con,cav},(1,2)}$), in the bottom row of figure 7, indicate that connected components in the Molino galaxy field become more isotropic compared to the dark-matter field, while cavities become less isotropic at all thresholds. This suggests that galaxy bias modifies not only the abundance of topological structures, but also their object-level morphology: overdense galaxy structures appear slightly more compact and isotropic, whereas underdense regions are sampled less uniformly and therefore appear more anisotropic. The dichotomy in shapes of connected components and cavities (cf. red and blue curves, lower middle panels of figure 7) seems to be directly related to the degree of non-Gaussianity in the field.

8 Shot noise

Shot noise is an important systematic for morphological statistics. The mean particle separation $\bar{r} = \bar{n}^{-1/3}$ is a limit below which shot noise significantly impairs our ability to reconstruct a continuous field from an underlying point distribution. Conversely, to maximize

JCAP08(2026)082

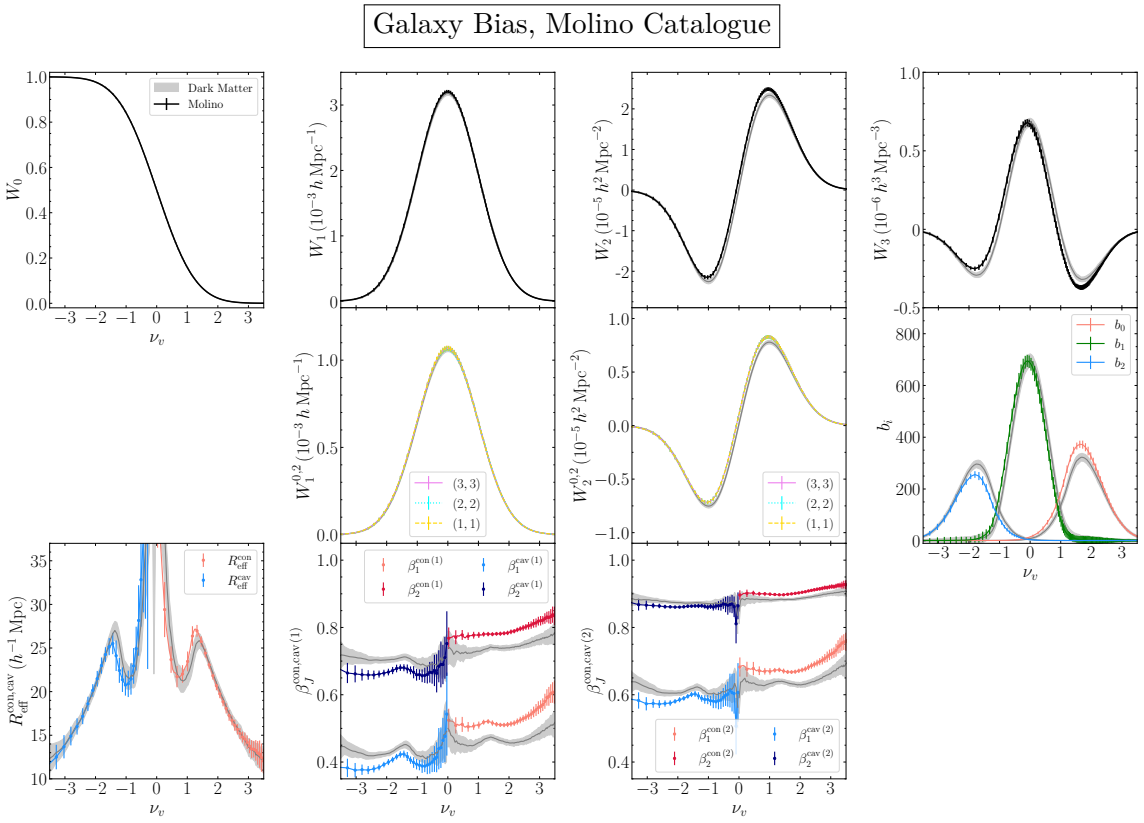


Figure 7. Morphological statistics measured for molino mock galaxy fields in real space. Coloured curves show the galaxy data, while the grey curves correspond to the fiducial dark matter fields and are included for comparison. Both fields are smoothed at $R_G = 20\,h^{-1}\,\mathrm{Mpc}$, reflecting the sparser mock galaxy sample with mean separation $\bar{r} \simeq 18\,h^{-1}\,\mathrm{Mpc}$. The panel layout and colour scheme follow figure 3.

the information content of the field we should smooth on the smallest scales available to us, which implies that we should generally select $R_G \sim \bar{r}$. This choice always places us in a regime where shot noise has a measurable impact on summary statistics like those studied in this work.

For a Gaussian random field, shot noise modifies the amplitudes of the Minkowski functionals by changing the spectral moments of the smoothed field, in particular increasing both σ_0 and σ_1. In this limit, an analytic Gaussian correction to the Minkowski functionals can be derived. For the gravitationally evolved matter field at $z = 0$, the density field is highly non-Gaussian, and the shot noise component can be similarly calculated in the higher point cumulants [102]. In this work we investigate the qualitative impact of shot noise on the MFs numerically, by contrasting our fiducial dark matter fields with an inter-particle separation of $\bar{r} = 2\,h^{-1}\,\mathrm{Mpc}$ with a randomly sampled, sparse DM distribution with $\bar{r} = 10\,h^{-1}\,\mathrm{Mpc}$. Both fields are smoothed with $R_G = 10\,h^{-1}\,\mathrm{Mpc}$.

The predominant consequence of shot noise is a systematic increase in the amplitudes of the Minkowski functionals, as shown in the four panels of the top row of figure 8. Physically, this behaviour can be understood as a consequence of shot-noise-induced excess variance in the reconstructed density field. Sparse sampling introduces small-scale stochastic features, which enhance the gradients and curvatures of the field and thereby modify the amplitudes

JCAP08(2026)082

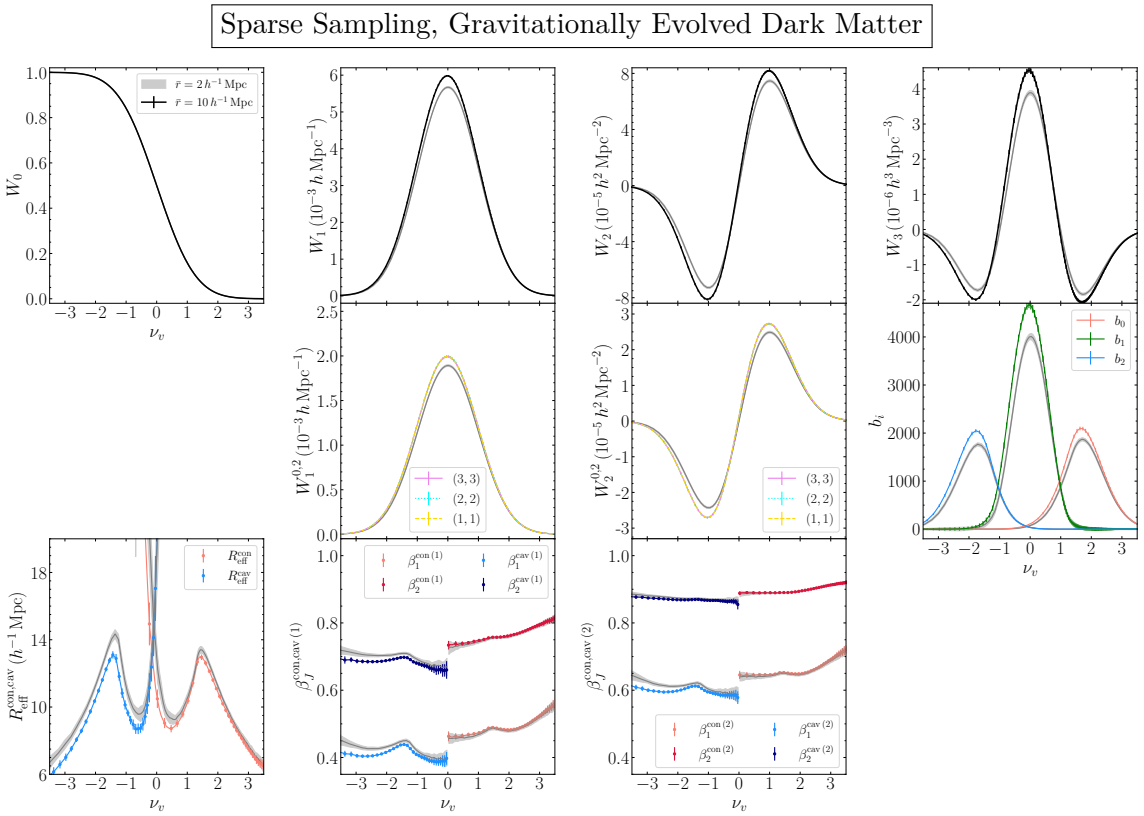


Figure 8. Morphological statistics measured for sparsely sampled dark matter fields in real space. Coloured curves show the sparsely sampled $\bar{r} = 10\,h^{-1}\,\mathrm{Mpc}$ case, while the grey curves correspond to the fiducial, dense fields with $\bar{r} = 2\,h^{-1}\,\mathrm{Mpc}$ from figure 3 and are included for comparison. The panel layout and colour scheme follow figure 3.

of the MFs. The diagonal MT components, shown in the middle-row panels of figure 8, remain statistically indistinguishable, with the sparse sampling producing mainly an overall amplitude increase. The Betti numbers are the most visibly affected by shot noise, indicating that topological quantities are particularly sensitive to discreteness-induced fluctuations. Shot noise has the effect of partially Gaussianizing the statistics, with the MF and Betti curves becoming less skewed for the sparsely sampled fields compared to the denser sample.

The local morphological statistics also show a detectable imprint of shot noise. The effective radii of cavities decrease, as indicated by the blue curve in bottom left panel of figure 8, while the sizes of connected components are only weakly affected (red curves). The shape parameters $\beta_J^{(1,2)}$ presented in middle panels, bottom row in figure 8 show a similarly systematic response: cavities become less isotropic, whereas connected component shapes are largely unchanged. The conclusion is that the predominant effect of shot noise is to create a larger number of smaller and more anisotropic cavities.

9 Parameter sensitivity

Finally, for the dark matter fields in real space, we explore the sensitivity of the global and local statistics to cosmological parameters. The Minkowski Functionals are finding increasing

JCAP08(2026)082

Parameter	Ω_m	σ_8	n_s
Fid	0.3175	0.834	0.9624
Ω_m^+	**0.3275**	0.834	0.9624
Ω_m^-	**0.3075**	0.834	0.9624
σ_8^+	0.3175	**0.849**	0.9624
σ_8^-	0.3175	**0.819**	0.9624
n_s^+	0.3175	0.834	**0.9824**
n_s^-	0.3175	0.834	**0.9424**

Table 1. Cosmological Models used in this work. Other cosmological parameters are fixed as $\Omega_b = 0.049$, $h = 0.6711$. Bold values indicate the parameter being varied from the fiducial.

application in cosmology [9, 18, 20, 21, 23, 47, 48, 51, 73, 80, 81], and here we consider the response of a broader family of summary statistics to the cosmological parameters Ω_m, n_s and σ_8. We restrict our analysis to this subset, assuming that tighter constraints on Ω_b and h will arise from complementary cosmological data.

To proceed, we use $N = 50$ realisations of the Quijote simulations for a set of different cosmological models, the parameters of which are presented in table 1. To estimate the parameter sensitivity, we first define the derivative of each statistic Y_k, at each threshold and for each realization, using the standard finite-difference scheme:

$$\frac{\partial Y_k}{\partial \theta} = \frac{Y_k(\theta^+) - Y_k(\theta^-)}{\theta^+ - \theta^-}, \tag{9.1}$$

where $\theta^\pm$ are the values of the parameters listed in table 1. In this section, we revert to the iso-field threshold ν, rather than ν_v. We worked with ν_v threshold in the previous sections to qualitatively study the response of morphology and topology to various phenomena, effectively removing the skewness of the purely local one-point function. In this section, we however aim to quantify the information content of the summary statistic curves in the Fisher information sense. Since the one-point skewness itself is sensitive to cosmological parameters, and we seek to maximize the parameter sensitivity, we return to the ν parameterization.

The results for the global and local statistics are shown in figure 9. The blue/red/green lines with shaded regions represent the mean and the error on the mean of the sensitivities to n_s, Ω_m and σ_8, respectively. In the middle panels of figure 9, which show $\partial W_1^{0,2}/\partial\theta$ and $\partial W_2^{0,2}/\partial\theta$, there are three distinct line styles (solid, dashed, dotted) for each colour. These correspond to the three diagonal components of the Minkowski tensors, but are not visually distinguishable as they overlap within the error bars, as expected for statistically isotropic fields.

In the top panels of figure 9, the blue and red curves differ primarily by an overall amplitude, indicating a strong degeneracy between n_s and Ω_m. This is a generic property of the Minkowski Functionals: their shapes are largely determined by a small number of one-point cumulants on quasi-linear scales $R_G \simeq 10\,h^{-1}\,\mathrm{Mpc}$. These cumulants depend on the shape of the matter power spectrum, and over a limited range of scales, variations of n_s and Ω_m can mimic one another, creating the observed degeneracy. There are two potential ways to break this degeneracy. The first is to combine measurements on relatively small

JCAP08(2026)082

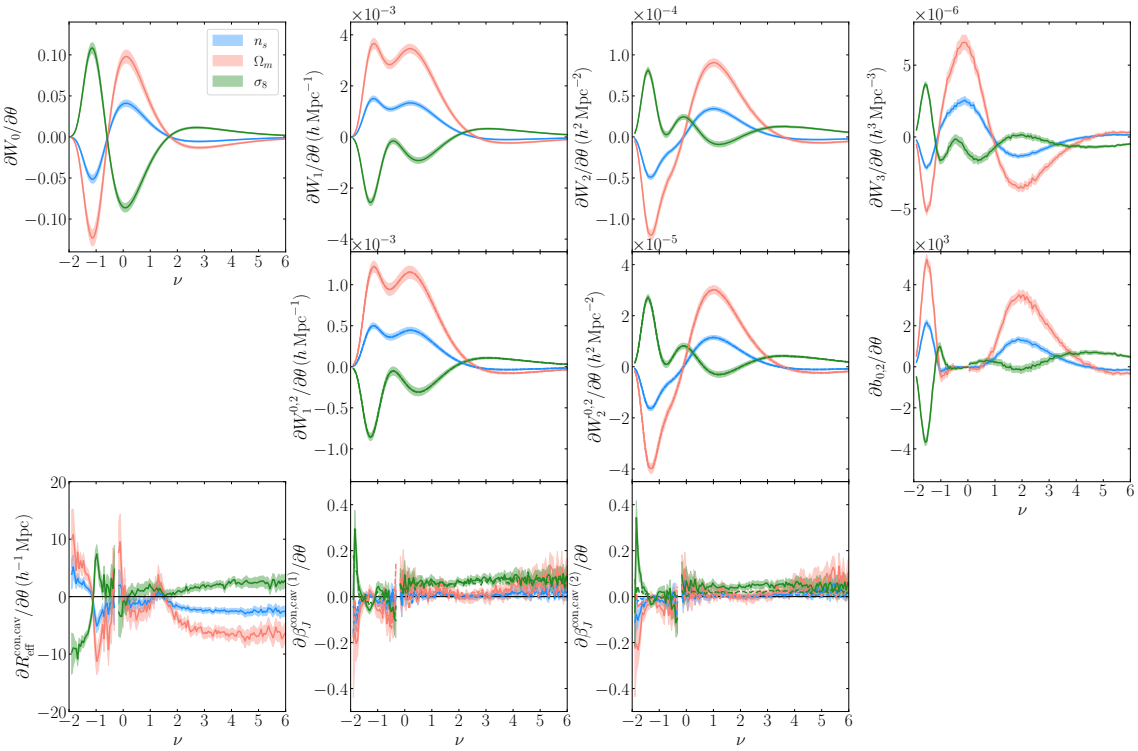


Figure 9. Sensitivity of the statistics to cosmological parameters n_s, Ω_m and σ_8 (blue/red/green bands). The lines/filled regions represent the mean/error on the mean of $N = 50$ realisations of each parameter set.

($R_G \sim 10\,h^{-1}\,\mathrm{Mpc}$) and large ($R_G \sim 30\,h^{-1}\,\mathrm{Mpc}$) smoothing scales, although the latter would suffer more from cosmic variance. The second is to adaptively smooth the field using a multi-scale kernel, which preserves the small scale information and probe the field in a regime in which perturbation theory breaks down.

In the Gaussian limit, the Minkowski functionals are independent of σ_8, which merely scales the amplitude of density fluctuations. By contrast, for gravitationally evolved, non-Gaussian fields, variations in σ_8 do more than rescale the amplitude; they also encode the degree of non-Gaussianity in the field. This difference explains the qualitatively distinct behaviour of the green curves relative to the blue and red ones. The effect is most clearly seen in the derivatives $\partial W_{1,2,3}/\partial\theta$ with respect to n_s and Ω_m, which include a term proportional to $W_{1,2,3}$. This proportionality indicates that these derivatives retain a substantial fraction of Gaussian information. In contrast, W_0 carries no cosmological information in its Gaussian expectation value, and therefore the curves for $\partial W_0/\partial\theta$ shown in the top-left panel arise entirely from non-Gaussian contributions.

In the second row of figure 9, the first two panels present the parameter sensitivity of the Minkowski Tensors. For each colour, the three curves (solid, dotted, dashed) represent the $(1,1)$, $(2,2)$, $(3,3)$ diagonal components, but they overlap entirely. The shapes of these curves match the corresponding MF curves above, indicating that no additional information is gained from the tensors when the field is isotropic. The Betti curves, shown in the right panel of the second row, do exhibit some additional discriminatory power. To avoid

JCAP08(2026)082

clutter, we only present $\partial b_2/\partial\theta$ and $\partial b_0/\partial\theta$ for negative/positive thresholds respectively, and omit $\partial b_1/\partial\theta$. The coloured curves show some variation in shape; for example, $\partial b_2/\partial\sigma_8$ (cf. green curve at negative thresholds) shows a secondary bump at $\nu \sim -1$ which is not discernable in the other cases.

In the bottom panels of figure 9, we present the parameter sensitivity of the local statistics $R_{\rm eff}^{\rm con,cav}$, $\beta_J^{\rm con,cav\,(1)}$, $\beta_J^{\rm con,cav\,(2)}$. For clarity, we show these quantities for $\nu > 0.2$ for connected components and $\nu < -0.3$ for cavities. In the left panel, we observe that variations in the cosmological parameters generate an almost constant shift in $R_{\rm eff}^{\rm con}$ for $\nu > 1.4$. At lower thresholds $\nu \lesssim 1.4$, where the connected components develop more complex topology, the sensitivity of $R_{\rm eff}^{\rm con}$ to cosmological parameters becomes weaker. For cavities (cf. $R_{\rm eff}^{\rm cav}$, $\nu < 0$), the percolating regime does retain some cosmological parameter dependence. However, the blue, red and green curves all have similar shapes up to an overall amplitude and sign, indicating that this quantity also exhibits strong degeneracies between cosmological parameters.

In the bottom middle and right panels, we show the parameter sensitivities of $\beta_J^{\rm con,cav\,(1)}$ and $\beta_J^{\rm con,cav\,(2)}$. The solid curves and shaded regions are the mean and error on the mean of $\beta_1^{\rm con,cav\,(1)}$ and $\beta_1^{\rm con,cav\,(2)}$, while the dashed lines (overlapping the solid lines) denote the means of $\beta_2^{\rm con,cav\,(1)}$ and $\beta_2^{\rm con,cav\,(2)}$. We find that both $\beta_J^{\rm con,cav\,(1)}$, $\beta_J^{\rm con,cav\,(2)}$ exhibit only weak sensitivity to the cosmological parameters across all thresholds probed. This indicates that the average ellipticity of connected components and cavities is a characteristic property of Gaussian and weakly non-Gaussian fields smoothed with a Gaussian kernel, and is not strongly sensitive to the detailed shape of the underlying power spectrum.

We quantify the degeneracy between different cosmological parameters in the sensitivity curves with the Fisher matrix. Specifically, we use $N = 1000$ realisations of the fiducial Quijote cosmological data to construct a 51×51 covariance matrix for the Y_k statistic as

$$C_{ij}^{(k)} = \frac{1}{N-1}\sum_{n=1}^{N}[Y_{k,n}(\nu_i) - \bar{Y}_k(\nu_i)]\,[Y_{k,n}(\nu_j) - \bar{Y}_k(\nu_j)], \tag{9.2}$$

where $Y_{k,n}(\nu_i)$ is the value of the Y_k statistic for the $n^{\rm th}$ realisation, in the $i^{\rm th}$ threshold bin and $\bar{Y}_k(\nu_i)$ is the realisation mean in the $i^{\rm th}$ threshold bin. We select 51 equi-spaced bins within the threshold range $-2 \le \nu \le 8$, and have checked that using a finer binning does not alter our results. Then, using the finite-difference sensitivities given by eq. (9.1), we define a dimensionless, normalised Fisher-like matrix

$$\hat{F}_{\mu\nu}^{(k)} = \frac{1}{A_{\mu\nu}}\left\langle\frac{\partial Y_k}{\partial\theta_\mu}\right\rangle(C^{(k)})^{-1}\left\langle\frac{\partial Y_k}{\partial\theta_\nu}\right\rangle, \tag{9.3}$$

where μ, ν run over the three cosmological parameters, $\langle\cdot\rangle$ denote average over $\mathbf{N = 1000}$ realizations, and the normalisation factor is defined as

$$A_{\mu\nu} = \sqrt{\left(\left\langle\frac{\partial Y_k}{\partial\theta_\mu}\right\rangle(C^{(k)})^{-1}\left\langle\frac{\partial Y_k}{\partial\theta_\mu}\right\rangle\right)\left(\left\langle\frac{\partial Y_k}{\partial\theta_\nu}\right\rangle(C^{(k)})^{-1}\left\langle\frac{\partial Y_k}{\partial\theta_\nu}\right\rangle\right)}. \tag{9.4}$$

By construction, the diagonal elements of $\hat{F}_{\mu\nu}^{(k)}$ are unity, and the off-diagonal elements represent the parameter correlation coefficients. Specifically, we define the off-diagonal

JCAP08(2026)082

	W_0	W_1	W_2	W_3	$W_1^{0,2}\|_1^1$	$W_2^{0,2}\|_1^1$	b_0	b_2
$\cos\theta_{\Omega_m n_s}$	0.9966	0.9891	0.9910	0.9837	0.9955	0.9920	0.9772	0.9392
$\cos\theta_{\Omega_m \sigma_8}$	−0.9139	−0.5397	−0.5173	−0.5333	−0.7433	−0.5566	−0.0850	−0.8496
$\cos\theta_{n_s \sigma_8}$	−0.9311	−0.6483	−0.6161	−0.6211	−0.7897	−0.6492	−0.1684	−0.8512
FoM	680	2510	2550	3880	1440	2100	2350	3590

Table 2. Correlations between the three parameters varied in this section — Ω_m, n_s and σ_8, extracted from the global statistics. The figure of Merit (fourth row) is a proxy for the overall information content of each individual statistic.

	$R_{\rm eff}^{\rm con}$	$\beta_1^{\rm con(1)}$	$\beta_2^{\rm con(1)}$	$\beta_1^{\rm con(2)}$	$\beta_2^{\rm con(2)}$	$R_{\rm eff}^{\rm cav}$	$\beta_1^{\rm cav(1)}$	$\beta_2^{\rm cav(1)}$	$\beta_1^{\rm cav(2)}$	$\beta_2^{\rm cav(2)}$
$\cos\theta_{\Omega_m n_s}$	0.9770	0.7991	0.7021	0.6218	0.6914	0.9744	0.8565	0.5859	0.8027	0.4309
$\cos\theta_{\Omega_m \sigma_8}$	−0.7970	0.1600	0.2724	0.1586	−0.0191	−0.7669	−0.2634	−0.2635	−0.3402	−0.4179
$\cos\theta_{n_s \sigma_8}$	−0.8135	0.0294	0.1311	0.0727	−0.0505	−0.7748	−0.3257	−0.4451	−0.3006	−0.6656
FoM	525	361	433	363	493	713	403	412	539	327

Table 3. Same information as in table 2, but for the local statistics.

elements as $\cos\theta_{\mu\nu}$, which corresponds to the cosine of the angle between sensitivity vectors $\partial Y_k/\partial\theta_\mu$ and $\partial Y_k/\partial\theta_\nu$ in the C^{-1} weighted space. A value close to $\cos\theta_{\mu\nu} \sim \pm 1$ indicates a strong degeneracy between parameters μ and ν. In table 2, we present the parameter degeneracies extracted from the global statistics, and in table 3, we list the same quantities for the local statistics. For the local statistics and b_0, b_2, we restrict our analysis to 25 bins over the range $-2 \leq \nu \leq 0$ (for cavities, b_0) and $0 \leq \nu \leq 8$ (for connected components, b_2). Finally, we present the figure of merit (FoM) of the un-normalised Fisher information matrix defined as:

$$F_{\mu\nu}^{(k)} \equiv \left\langle \frac{\partial Y_k}{\partial\theta_\mu} \right\rangle (C^{(k)})^{-1} \left\langle \frac{\partial Y_k}{\partial\theta_\nu} \right\rangle , \tag{9.5}$$

$$\mathrm{FoM}_k = \left[\det F^{(k)}\right]^{1/3} , \tag{9.6}$$

where FoM is a proxy for the information contained in the various statistics. Although the FoM extracted from snapshot boxes is not directly relevant for observational constraints, we can use this quantity to compare the relative information contained in the various statistics measured in this work.

We stress that the purpose of this section is not to use the Fisher-like matrix $\hat{F}_{\mu\nu}^{(k)}$ defined in eq. (9.3) as a tool for cosmological parameter forecasting. A rigorous Fisher analysis should pertain to a specific survey, with a specified galaxy bias, number density, footprint and angular selection function. Such an analysis will be considered elsewhere, and will require the careful construction of mock galaxy catalogues representative of ongoing and next-generation

JCAP08(2026)082

surveys. Rather, our objective here is to quantify the response of our statistics to various cosmological parameters. Quantities such as the MFs represent an extreme compression of data, from the full three-dimensional field down to four curves W_0-W_3 as functions of the threshold ν. Furthermore, on quasi-linear scales where the Edgeworth expansion can be used, these curves are controlled by a small number of $\sim\mathcal{O}(10)$ field cumulant ratios. In this section, we use the $\hat{F}^{(k)}$ matrices to determine what discriminatory power survives this enormous data compression, and to investigate whether combining distinct topological statistics can break the parameter degeneracies that are clearly visible in figure 9.

In table 2, we first observe a strong positive correlation between Ω_m and n_s (cf. first row), which is present for all the global statistics. By restricting our analysis to a single smoothing scale $R_G = 10\,h^{-1}\,\mathrm{Mpc}$, we cannot disentangle the morphological effects of a net tilt in the power spectrum from a physical shift in the peak of the matter density field. The amplitude σ_8 is negatively correlated with the combination Ω_m and n_s, though not perfectly, which indicates that measurements of combinations of the global statistics will yield constraints in the $(\sigma_8, \Omega_m \times n_s)$ plane of our three-dimensional parameter space. Furthermore, the figures of Merit (fourth row) informs us that the relative constraining power increases in the order of, $W_0 < W_1 \sim W_2 < W_3$. We only present a single component of the Minkowski tensors, but the combination of three diagonal elements of $W_1^{0,2}$ and $W_2^{0,2}$ contains practically the same constraining power as W_1 and W_2 respectively. Finally, the Betti numbers are the most interesting of all the global statistics, due to their combination of constraining power and rotated parameter degeneracies compared to the Minkowski functional W_3.

In table 3, we present the same information, but for the individual connected component and cavity statistics. First, we note that the parameter degeneracies have rotated, with $\cos\theta_{\Omega_m n_s} \sim 0.4$–$0.8$ for the shape statistics β and a positive correlation between σ_8 and Ω_m, n_s. Consequently, measuring a combination of local and global statistics can effectively break the degeneracies seen in the Minkowski Functionals. In appendix C, we explicitly show that in the high threshold limit of a Gaussian random field, the local statistics $R_{\mathrm{eff}}^{\mathrm{con}}$ and $\beta_J^{\mathrm{con}\,(1,2)}$ are sensitive to ratio $\gamma = \sigma_1^2/\sigma_0\sigma_2$, whereas the Minkowski functionals extracted from the same fields are only sensitive to the ratio σ_1/σ_0.

However, while the local statistics can help to break the degeneracies present in the global statistics, the individual information contained in these curves, characterized by their figure of merit, is significantly lower. This is because they de-weight the largest objects in the average, and it is the largest excursion set boundaries that carry the most information in the global statistics. A rigorous cosmological parameter forecast using realistic mock galaxy survey will be required to determine precisely how effectively these local morphological statistics can optimize parameter estimation in the presence of observational systematics.

10 Discussion

10.1 Summary of results

We have investigated three different cosmological effects: non-linear gravitational collapse, redshift space distortion (RSD) and massive neutrino free streaming, and studied their imprints on the morphology of three-dimensional matter density fields. Using a set of global

JCAP08(2026)082

and local morphological descriptors including the Minkowski Functionals, Minkowski Tensors, Betti numbers, and the effective radius and shape of connected components and cavities, we have shown that each process imprints a characteristic and qualitatively distinct signature on excursion-set geometry and topology.

Gravitational collapse primarily induces non-Gaussianity through mode coupling, leading to skewness in the Minkowski Functional curves and significant modifications to the Betti numbers, while preserving statistical isotropy at the global level. Massive neutrinos suppress small-scale power in an isotropic fashion, leading to subtle changes; primarily modifying one-point cumulants and decreasing the amplitude of the MFs. In contrast, redshift-space distortions strongly modify the shapes of individual excursion sets and directionally sensitive global measures such as the MTs.

The percolation of the field from high to low thresholds imprints a particular pattern on the average size and shape of individual connected components and cavities (cf. bottom panels, figure 1). The peaks at $\nu = \pm 1.4$ correspond to the threshold at which large excursion sets amalgamate, and is slightly lower than the locations of peaks of the Betti numbers b_0 and b_2. The position of the peaks, and in particular the shape of the $R_{\rm eff}^{\rm con}$ curve, is practically unaffected by gravitational collapse, redshift space distortion and the presence of massive neutrinos, after the one point skewness of the field has been removed. It is possible that the peak position could be estimated using an ellipsoid packing algorithm. The shape statistics $\beta_J^{\rm con,cav\,(1,2)}$ are modified by gravitational collapse and redshift space distortion, in particular the connected components are both systematically more spherical in real space as a result of gravitational evolution while simultaneously being elongated marginally by redshift space distortion, with the largest effect at high thresholds. The shape of the cavities, as characterised by $\beta_J^{\rm cav\,(1,2)}$, are largely unchanged by the processes studied in this work, becoming marginally more anisotropic due to gravitational evolution.

10.2 Comparison with previous work

Minkowski functionals have been widely used to quantify non-Gaussianity and non-linear structure formation in the matter and galaxy distributions, and have been shown to complement two-point statistics by capturing one-point information. More recently, Minkowski tensors have been developed and applied as a natural extension of scalar Minkowski functionals, providing direct sensitivity to directional information and anisotropy.

Our findings are consistent with earlier investigations of topology of LSS of the universe but extend them in several directions. A direct parallel can be drawn between our results and the earlier topological analysis of [92], where authors examined how gravitational evolution, biasing, and redshift-space distortions modify the genus statistic. They found that gravitational nonlinearity significantly alters the topology by reducing the number of isolated high-density regions and enhancing void merging; trends fully consistent with our Betti-numbers and effective-radius results. Their conclusion that RSD lowers the genus amplitude without significantly altering its qualitative shape mirror our finding that RSD suppresses Minkowski Functionals and produces strong anisotropy captured by the Minkowski Tensors. Thus, our findings not only corroborate the trends identified in [92] but also extend them by incorporating an expanded set of morphological statistics. Our RSD analysis builds

JCAP08(2026)082

on earlier work demonstrating the ability of Minkowski Tensors to capture anisotropy induced by coherent flows and virial motions due to peculiar velocities [74, 86]. Our results show that redshift space introduces a measurable anisotropy in the Minkowski Tensors, with the line-of-sight component deviating significantly from the transverse components, breaking the degeneracy seen in real space.

The morphological impact of massive neutrinos has been explored in a limited number of previous works, primarily using Minkowski Functionals applied to weak-lensing fields [81, 111] or three-dimensional matter and galaxy density fields [47, 48]. These studies focus on parameter inference and demonstrate that combining morphological statistics with the power spectrum or bispectrum can significantly improve constraints on the sum of neutrino masses. In contrast, the focus of our analysis is on developing a qualitative understanding of how different cosmological effects modify the excursion-set morphology. Within this framework, we find that massive neutrinos leave the Minkowski Tensors isotropic, introduce only mild but systematic changes in the MFs and Betti numbers, primarily due to the suppression of small scale power. At the typical tracer separations of existing galaxy catalogues $\bar{r} \sim 10\,h^{-1}\,\mathrm{Mpc}$, the neutrino signal is extremely subtle. Moreover, the competing effects of gravitational evolution, shot noise, galaxy bias make the extraction of competitive neutrino-mass constraint from these statistics challenging. A multi-scale probe of the density field would allow us to better study the impact of neutrino mass and will be considered elsewhere.

10.3 Sensitivity of morphological statistics to cosmology

Our analysis shows that the global morphological statistics, particularly the amplitudes of the Minkowski Functionals, are sensitive to variations in cosmological parameters such as Ω_m, n_s and σ_8. While Ω_m and n_s modify the shape of the matter power spectrum, σ_8 rescales the overall amplitude of density fluctuations. These changes lead to coherent modifications in the geometry and topology of excursion sets. A detailed cosmological parameter analysis exploiting these sensitivities will be presented in a forthcoming study.

The local statistics — effective radius $R_{\mathrm{eff}}^{\mathrm{con,cav}}$ and shape parameters $\beta_J^{\mathrm{con,cav}\,(1,2)}$ — exhibit lower sensitivity to cosmological parameter variations. Crucially, however, they exhibit rotated parameter degeneracies compared to the global statistics making them potentially useful complementary tools for joint parameter inference. These local descriptors are visibly affected by the key physical effects examined here: non-linear gravitational collapse produces marked asymmetries between overdense and underdense regions, while RSD generates measurable anisotropic distortions of size and shape of structures. Their sensitivity to such physical processes, despite their insensitivity to cosmological parameters, indicates that they probe complementary aspects of structure formation that are not captured by global, averaged morphological measures. Ultimately, these local statistics provide genuinely novel information compared to their global counterparts, due to the fact that the averaging over connected components and cavities down-weights the largest objects that dominate the Minkowski Functionals. This difference is explored further in appendix B.

Regarding the cosmological parameter sensitivity of the MFs, we note that our sensitivity curves $\partial Y_k/\partial\theta$ differ in shape compared to other work in the literature [47, 48]. Those works use a different threshold $\nu = \rho/\bar{\rho} = 1 + \delta$ to define excursion sets, where $\bar{\rho}$ is the mean

JCAP08(2026)082

density of the field. This should be compared to our choice $\nu = \delta/\sigma_0$. The difference is not simply a common re-scaling of the x-axis for non-Gaussian fields, and will change the structure of the curves as we vary the cosmological parameters. Although any reasonable choice of excursion set thresholding can be used, and in fact the one adopted in [47, 48] may help to break certain parameter degeneracies, we choose the definition for which theoretical results are typically calculated [36].

10.4 Limitations & future work

The present analysis is restricted to dark-matter-only simulations and idealized density fields. Extensions to realistic survey geometries and angular selection functions will be essential for direct application to observational data. In addition, while we have explored the response to a subset of cosmological parameters, future work will focus on joint inference using full covariance information and likelihood-based and machine-learning-driven approaches.

Acknowledgments

PG is supported by KIAS Individual Grant (PG088101) at Korea Institute for Advanced Study (KIAS). SA is supported by a KIAS Individual Grant (PG055703) at Korea Institute for Advanced Study (KIAS). PC gratefully acknowledges the support of a visiting professorship at KIAS, during which part of this work was carried out. CBP is supported by the National Research Foundation of Korea (NRF) grant funded by the Korean government (MSIT; RS-2024-00360385).

A Effect of gravitational evolution

As stated in section 4, the overwhelming effect of gravitational collapse is to skew the density threshold ν, as seen for example in the top-left panel of figure 2 showing W_0, whose shape traces the cumulative probability distribution function (CPDF). Gravitational collapse changes the one-point function of the density field from a Gaussian form to one that is highly skewed towards large positive values. The non-Gaussianity in the one-point function is eliminated in section 4 via a $\nu \to \nu_v$ threshold transformation.

In figure 10, we present ν_v as a function of ν for the $z = 0$ dark matter density field in real space (solid black curve), in redshift space (red dashed curve), and in real space with a massive neutrino component (blue dotted curve). These curves fully characterize the evolution of the density field PDFs from Gaussian to skewed distributions. The Gaussian expectation, $\nu_v = \nu$, is shown by the grey line for reference.

B Information content of the local statistics

Here we briefly outline how ensemble averages of the Minkowski functionals and tensors differ from averages over the morphology of individual connected components or cavities. We focus on $R_{\rm eff}^{\rm con}$ and W_0, as they are the simplest statistics that can be used to demonstrate this distinction. The key difference arises because, although both $R_{\rm eff}^{\rm con}$ and W_0 can be expressed as averages over excursion sets, only W_0 can additionally be written as a volume average

JCAP08(2026)082

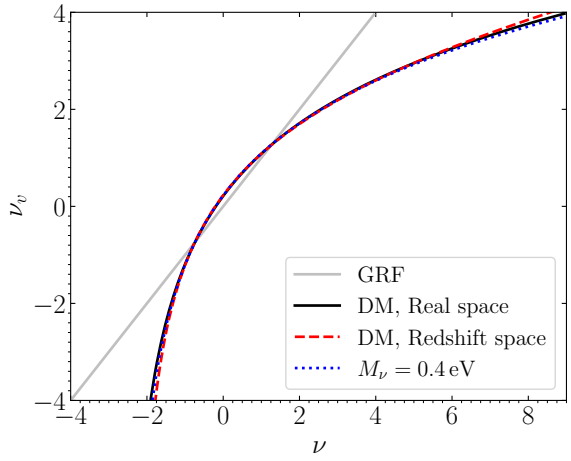


Figure 10. Volume fraction threshold ν_v presented as a function of iso-field threshold ν for the $z = 0$, real space dark matter fields (black curve) and Gaussian random fields (grey curve).

over pixels. Consequently, for W_0, ensemble and volume averages commute, whereas for $R_{\rm eff}^{\rm con}$ they do not.

For simplicity, we consider Gaussian random fields here. Let us recall the definition of $R_{\rm eff}^{\rm con}$:

$$R_{\rm eff}^{\rm con} = \frac{1}{b_0}\left(\frac{3}{4\pi}\right)^{1/3}\sum_{i=1}^{b_0} x_i\,, \tag{B.1}$$

where b_0 is the number of connected components, and x_i is the cube root of the volume V_i of the ith connected component Q_i,

$$x_i = V_i^{1/3} = \left(\int_{Q_i} dV\right)^{1/3}. \tag{B.2}$$

Note that $R_{\rm eff}^{\rm con}$ is a function of the random variables b_0 and x_i. We also recall that W_0 is given by:

$$W_0 = \frac{1}{V}\sum_{i=1}^{b_0} V_i\,, \tag{B.3}$$

and is therefore a function of the random variables V_i.

The ensemble averages of $R_{\rm eff}^{\rm con}$ and W_0 are given by

$$\langle R_{\rm eff}^{\rm con}\rangle = \left(\frac{3}{4\pi}\right)^{1/3}\left\langle\frac{1}{b_0}\sum_{i=1}^{b_0} x_i\right\rangle = \left(\frac{3}{4\pi}\right)^{1/3}\sum_{n\geq 1} P(b_0 = n\,|\,V)\left\langle\frac{1}{n}\sum_{i=1}^{n} x_i\Big|b_0 = n\,,\,V\right\rangle \tag{B.4}$$

$$= \left(\frac{3}{4\pi}\right)^{1/3}\sum_{n\geq 1} P(b_0 = n\,|\,V)\,\langle x_1|b_0 = n\,,\,V\rangle\,, \tag{B.5}$$

$$\langle W_0\rangle = \frac{1}{V}\left\langle\sum_{i=1}^{b_0} V_i\right\rangle = \frac{1}{V}\sum_{n\geq 1} P(b_0 = n|V)\left\langle\sum_{i=1}^{n} V_i\Big|b_0 = n,\,V\right\rangle \tag{B.6}$$

$$= \frac{1}{V}\sum_{n\geq 1} P(b_0 = n|V)\,n\,\langle V_1|b_0 = n,\,V\rangle\,. \tag{B.7}$$

JCAP08(2026)082

In the above, we have decomposed the ensemble averages into contributions conditional on b_0 while keeping the total volume V finite. The quantity $P(b_0 = n|V)$ denotes the probability of n connected components contained within a volume V. In eqs. (B.5), (B.7) we have commuted the sums over n and the ensemble averages, and then reduced the sums to n-copies of $\langle x_1|b_0 = n, V\rangle$ and $\langle V_1|b_0 = n, V\rangle$. This last step can be taken because the joint distribution of $\{x_i\}$ (or $\{V_i\}$), conditioned on $b_0 = n$, is invariant under permutations of the index i, which allows the sum to be reduced to n identical conditional expectations.

For W_0, we can re-write the sum over excursion sets as the sum over pixels as

$$\sum_{i=1}^{b_0} V_i = \sum_{i=1}^{N_{\rm pix}} \Delta^3 \Theta(\delta_i - \nu) \tag{B.8}$$

where $\Theta(x)$ is the Heaviside function and Δ^3 is the pixel size. With this re-writing, the only random variables after the first equality of eq. (B.6) are the pixel values δ_i in the Heaviside function (and specifically the sum is now over the deterministic quantity $N_{\rm pix}$), so the ensemble average commutes with the sum and we can write

$$\langle W_0\rangle = \frac{\Delta^3}{V} \sum_{i=1}^{N_{\rm pix}} \int_{-\infty}^{\infty} P(\delta_i)\Theta(\delta_i - \nu){\rm d}\delta_i \,, \tag{B.9}$$

from which the standard result follows — the sum is simply $N_{\rm pix}$ copies of the one point integral of the density field PDF integrated over the range (ν, ∞), and we can take the limits $N_{\rm pix} \to \infty$, $V = N_{\rm pix}\Delta^3 \to \infty$.

The reason why we can exactly calculate $\langle W_0\rangle$ is the linearity of the sum, and the fact that we can re-write the sum over excursion set volumes as a sum over all pixels. This is because W_0 contains no information about correlations between pixel values, it depends only on whether each pixel is 'in' or 'out' of the excursion set.

Although the expression (B.5) is exact for $\langle R_{\rm eff}^{\rm con}\rangle$, it cannot be reduced further to a simple closed form like $\langle W_0\rangle$ in eq. (B.9). If we assume that b_0 and V_i are independent variables, and V_i are independent and identically distributed (iid), then we could proceed by writing (B.5) as:

$$\langle R_{\rm eff}^{\rm con}\rangle = \left(\frac{3}{4\pi}\right)^{1/3} \langle x_1 \,|\, V\rangle \,. \tag{B.10}$$

That is, under these assumptions $\langle R_{\rm eff}^{\rm con}\rangle$ would be a measure of a fractional moment $\langle V_1^{1/3}\rangle$ of the probability density function $P(V_1)$ of connected component volumes. However, the assumptions used to arrive at eq. (B.10) are not reliable over the entire density threshold range that we consider.

We examine these assumptions in turn. First, the number of connected components b_0 is correlated with the volume of individual elements V_i for all thresholds, and the correlation is particularly strong for $0 \lesssim \nu \lesssim 1.4$. At large thresholds $\nu > 2$, the correlation is weak and due to the constraint that the total volume of all connected components must equal W_0, so increasing b_0 forces the average volume of subsets to decrease. For low thresholds $0 \lesssim \nu \lesssim 1.4$, the excursion set is dominated by a small number of large-volume subsets together with many smaller disconnected regions. In this regime, the random variable b_0 is strongly influenced by the presence of these large structures, which start to form at $\nu \lesssim 1.4$.

JCAP08(2026)082

Second, for defining the ensemble average of the Minkowski Functionals, we take the limit $V \to \infty$. In terms of the ensemble average over b_0 (cf. eq. (B.5)), this would ideally correspond to the limit $\langle b_0 \rangle \propto V \to \infty$. In practice, we estimate summary statistics from finite-volume fields, and in the limits $\nu \gg 1$ and $\nu \lesssim 0$, we will measure only a small number of subsets. In particular, for $\nu \lesssim 1.4$, the sub-volumes merge into a small number of (or single) percolating structures, and it is unclear how well volume and ensemble averages will match. Similarly, for finite V we will always encounter a large threshold limit where the number of excursion sets is small. For both limits, we should compare measured averages from data with eq. (B.5), which makes no assumption about the size of V.

Finally, we turn to the assumption that x_i are iid. This is likely to be a good approximation for high thresholds where connected components are spatially well separated. In contrast, at $\nu \lesssim 1.4$, large volume subsets form and percolation occurs, in which case the distribution of x_i will be characterized by a small number of large volume connected components and more numerous, small volume islands. The large and small volume elements are neither independent nor identically distributed, making an estimate of $\langle x \rangle$ difficult.

To highlight these issues, in figure 11 we present the scatter plots of the effective radius $R_{\rm eff}^{\rm con}$ and the shape parameter $\beta_1^{{\rm con}\,(1)}$ for all connected components measured from $N_{\rm real} = 50$ realizations of real space Gaussian random fields using the same parameters and smoothing as in section 3. Each blue point corresponds to a single connected component, and each panel shows a different density threshold (top row, left to right: $\nu = 3, 2, 1.4$; bottom row, left to right: $\nu = 1.2, 0.8, 0.4$). The dark blue points with error bars show the binned mean and 1σ scatter. We display $\beta_1^{{\rm con}\,(1)}$ as representative of the four shape parameters measured in this work; the remaining three exhibit qualitatively similar behaviour.

Starting from a high threshold $\nu = 3$ (top left panel), the connected component are drawn from a relatively compact two-dimensional distribution with only weak correlation between $R_{\rm eff}^{\rm con}$ and $\beta_1^{{\rm con}\,(1)}$.[3] These objects are predominantly isolated peaks of the Gaussian field and are approximately independent realisations of a single population.

As the threshold is lowered, this simple picture breaks down. By $\nu = 1.4$ (top right panel) a second population of connected components emerges, characterised by substantially larger radii and higher values of $\beta_{1,i}^{{\rm con}\,(1)}$. These objects are no longer simple peak-like structures but are composite regions formed from chains of peaks connected by saddle critical points. The effective sizes of connected components are, therefore, no longer drawn from a single underlying distribution, and the assumption that they form an approximately iid ensemble becomes invalid.

Upon further decreasing the threshold (bottom row), a single percolating object appears in each realisation, visible as isolated points in the top-right corner of each panel. As ν decreases from 1.2 to 0.8 and 0.4 (left to right panels), this dominant object grows by absorbing an increasing fraction of the remaining smaller subsets. Hence for $\nu \lesssim 1.2$, the excursion set bifurcates into one extremely large region and an increasingly sparse population of smaller objects. The global Minkowski functionals W_0–W_3, being integrals over the entire excursion set volume/boundary, become dominated by the properties of the single percolating object at

[3] A small systematic trend of $\beta_1^{{\rm con}\,(1)}$ first decreasing then increasing with increasing $R_{\rm eff}^{\rm con}$ is visible in the binned averages.

JCAP08(2026)082

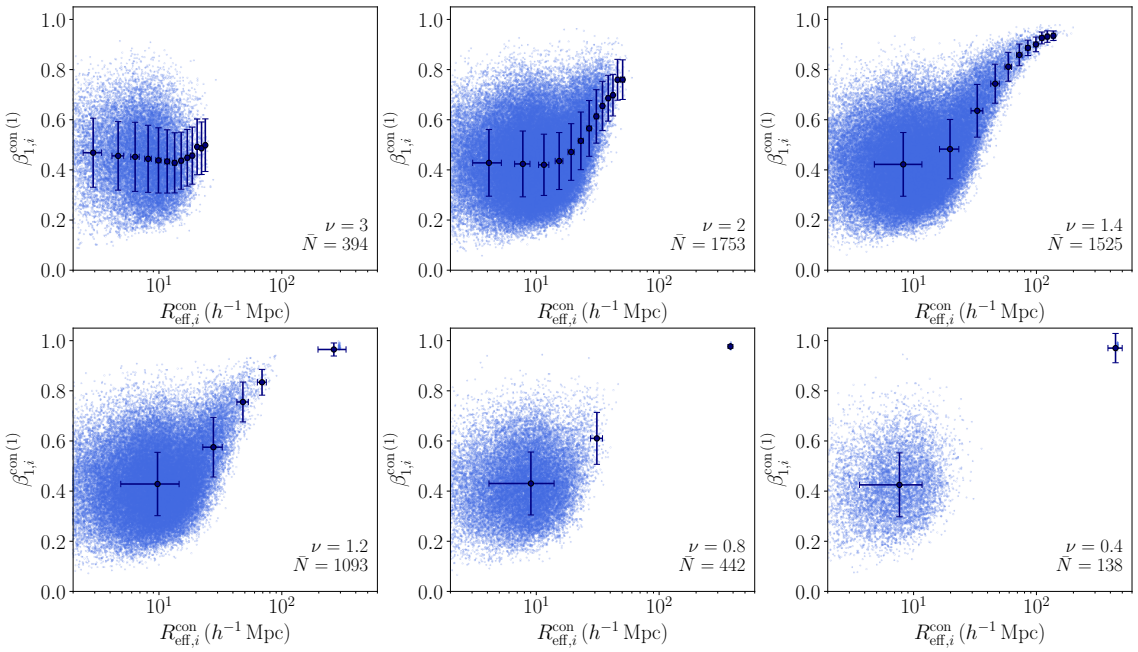


Figure 11. Two-dimensional distribution of $\beta_{1,i}^{\mathrm{con}\,(1)}$ and $R_{\mathrm{eff},i}^{\mathrm{con}}$ extracted from individual connected components from $N_{\mathrm{real}} = 50$ realisations of a Gaussian random field in real space (blue points). Each blue point represents a single excursion region from the realisations. The top row (left-right panels) are connected components at thresholds $\nu = 3, 2, 1.4$ and the bottom row $\nu = 1.2, 0.8, 0.4$. The dark blue points/errorbars are the mean and 1σ uncertainty of the binned point cloud.

$\nu \lesssim 1.2$, whereas local statistics such as the shape parameters $\beta_{J,i}^{\mathrm{con}\,(1,2)}$ probe predominantly the morphology of the small, peak-like point clouds.

The scatter plots shown in figure 11 make it explicit that below the percolation threshold the connected components cannot be treated as a homogeneous ensemble, which obfuscates the analytic modelling of their average morphological properties. However, one could introduce cuts, in $R_{\mathrm{eff}}^{\mathrm{con}}$ for example, to isolate connected components that are approximately iid and hence more amenable to analytic study.

The global statistics, being averages over the total iso-field boundary, are dominated by the properties of the largest objects in the excursion set. In contrast, the local statistics contain information in the small peaks represented by the point clouds in figure 11. Hence they provide additional information, arising from the average over connected components/cavities rather than the total boundary.

C High threshold ensemble average

We can use the local, elliptical peak approximation to estimate the expectation value of $\langle R_{\mathrm{eff}}^{\mathrm{con}} \rangle$, $\langle \beta_J^{\mathrm{con}\,(1)} \rangle$, and $\langle \beta_J^{\mathrm{con}\,(2)} \rangle$ at high thresholds. In this appendix, we restrict our analysis to Gaussian random fields in real space, for which the statistical properties of peaks are well studied [112–114].

A peak (located at some arbitrary point $\mathbf{r} = \mathbf{0}$) can be characterized by the field δ, and its first $\eta_i = \nabla_i \delta$ and second $\xi_{ij} = \nabla_i \nabla_j \delta$ derivatives at that point. In particular, a peak is defined

JCAP08(2026)082

by $\eta_i(\mathbf{0}) = 0$ and ξ_{ij} having three negative eigenvalues — these correspond to conditions on the joint ten-dimensional PDF $P(\delta, \eta_i, \xi_{ij})$ that can be partially marginalised over. We can write a local expansion of the density in the vicinity of a peak of height $\delta_{\rm pk}$ at $\mathbf{r} = \mathbf{0}$:

$$\delta(\mathbf{r}) = \delta_{\rm pk} + \frac{1}{2}\sum_{i,j=1}^{3} \xi_{ij} r^i r^j + \mathcal{O}(|\mathbf{r}|^3) \tag{C.1}$$

It is convenient to define all variables in dimensionless form as $\nu = \delta/\sigma_0$, $\tilde{\eta}_i = \eta_i/\sigma_1$ and $\tilde{\xi}_{ij} = -\xi_{ij}/\sigma_2$, where

$$\sigma_i^2 = \frac{1}{2\pi^2}\int k^{2+2i} dk P(k) W(kR_{\rm G})^2\,, \tag{C.2}$$

and we also define $\gamma = \sigma_1^2/(\sigma_0\sigma_2)$. We have used the standard convention of introducing a minus sign in the definition of $\tilde{\xi}_{ij}$ so that the eigenvalues for a peak are positive. Next we rotate the local coordinate system such that $\tilde{\xi}_{ij}$ is diagonal, with components corresponding to its eigenvalues $\lambda_1 \geq \lambda_2 \geq \lambda_3 > 0$, and define the following variables

$$x = \lambda_1 + \lambda_2 + \lambda_3\,, \quad e = \frac{\lambda_1 - \lambda_3}{2x}\,, \quad p = \frac{\lambda_1 - 2\lambda_2 + \lambda_3}{2x}\,. \tag{C.3}$$

In terms of these variables, the peak probability distribution of height $\nu_{\rm pk}$, and shape parameters x, e, p is given by [112, 114]

$$P_{\rm pk}(\nu_{\rm pk}, x, e, p) = A x^8 e^{-Q_{\nu x}(\nu_{\rm pk}, x)} e^{-Q_{ep}(x,e,p)} \mathcal{J}(e,p)\Theta(x,e,p), \tag{C.4}$$

where

$$Q_{\nu x}(\nu_{\rm pk}, x) = \frac{\nu_{\rm pk}^2 - 2\gamma\nu_{\rm pk}x + x^2}{2(1-\gamma^2)}\,, \qquad Q_{ep}(x,e,p) = \frac{5}{2}x^2(3e^2 + p^2)\,, \tag{C.5}$$

and

$$\mathcal{J}(e,p) = e(e^2 - p^2)(1-2p)\left[(1+p)^2 - 9e^2\right], \tag{C.6}$$

and

$$\Theta(x,e,p) = \begin{cases} 1 & \text{if } (0 \leq e \leq 1/4\,, \quad -e \leq p \leq e\,, \quad x > 0), \\ 1 & \text{if } (1/4 \leq e \leq 1/2 \quad 3e - 1 \leq p \leq e\,, \quad x > 0), \\ 0 & \text{otherwise.} \end{cases} \tag{C.7}$$

The normalisation factor, A, is defined such that the PDF integrates to unity, but cancels for the conditional probabilities that we will consider below.

For a given threshold $\delta(\mathbf{r}) = \nu\sigma_0$, we can re-write equation (C.1) as

$$\nu = \nu_{\rm pk} - \frac{\sigma_2}{2\sigma_0}\sum_i \lambda_i q_i^2, \tag{C.8}$$

with $\nu_{\rm pk} > \nu$ and q_i are the rotated coordinates aligned with the ellipsoid principal axes. The volume of the ellipsoid enclosed by ν can be inferred from this equation in terms of the variables ν, $\nu_{\rm pk}$, x, e, p:

$$V \simeq \frac{4\pi}{3}\left(\frac{2\sigma_0}{\sigma_2}\right)^{3/2}(\nu_{\rm pk} - \nu)^{3/2}\left(\frac{3}{x}\right)^{3/2}\frac{1}{\sqrt{(1+3e+p)(1-2p)(1-3e+p)}}. \tag{C.9}$$

JCAP08(2026)082

We can approximate the expectation value for $\langle R_{\rm eff}^{\rm con}\rangle$ as

$$\langle R_{\rm eff}^{\rm con}\rangle \simeq \frac{1}{N}\int_{\nu}^{\infty} {\rm d}\nu' \int {\rm d}x\,{\rm d}e\,{\rm d}p\, P_{\rm pk}(\nu', x, e, p) V^{1/3}, \tag{C.10}$$

$$N = \int_{\nu}^{\infty} {\rm d}\nu' \int {\rm d}x\,{\rm d}e\,{\rm d}p P_{\rm pk}(\nu', x, e, p). \tag{C.11}$$

If the majority of the peaks lie close to ν, and the number of filamentary saddle points with $\nu_{\rm sad} > \nu$ is much smaller than the number of peaks with $\nu_{\rm pk} > \nu$, then we can expect eq. (C.10) to provide a good approximation to the ensemble average. At thresholds for which the topology of excursion sets is non-trivial (a significant number of loops, for example) then this approximation will completely break down.

We note that $\langle R_{\rm eff}^{\rm con}\rangle$ is explicitly sensitive to the cumulant σ_2, which is present in V and also in $P_{\rm pk}(\nu, x, e, p)$ via the γ term. This highlights that the local statistics contains information that is not present in the scalar Minkowski functionals, which are only sensitive to the single ratio σ_1/σ_0 for a Gaussian field.

C.1 Local shape information

We can perform a similar calculation for the $\beta_J^{{\rm con}\,(1)}$, $\beta_J^{{\rm con}\,(2)}$ shape functions. Parameterizing the coordinates on the surface of an ellipsoid as $x = a\sin\theta\cos\phi$, $y = b\sin\theta\sin\phi$, $z = c\cos\theta$ with $0 \le \theta < \pi$ and $0 \le \phi < 2\pi$ and $a \le b \le c$, the unit normal components to the surface are obtained by taking the gradient of the implicit equation of the ellipse:

$$\hat{n}_x = \frac{\sin\theta\cos\phi}{\ell}, \quad \hat{n}_y = \frac{a}{b}\frac{\sin\theta\sin\phi}{\ell}, \quad \hat{n}_z = \frac{a}{c}\frac{\cos\theta}{\ell}, \tag{C.12}$$

$$\ell(\theta,\phi) = \left[\left(\frac{a}{c}\right)^2\cos^2\theta + \sin^2\theta\left(\cos^2\phi + \left(\frac{a}{b}\right)^2\sin^2\phi\right)\right]^{1/2}, \tag{C.13}$$

and the mean curvature of the surface is

$$G_2 = \frac{1}{2}\nabla.\hat{n} \tag{C.14}$$

$$= \frac{1}{2\,a}\left[\frac{1}{\ell(\theta,\phi)}\left(1 + \left(\frac{a}{b}\right)^2 + \left(\frac{a}{c}\right)^2\right) - \frac{1}{\ell(\theta,\phi)^3}\left(\left(\frac{a}{c}\right)^4\cos^2\theta + \sin^2\theta\left(\cos^2\phi + \left(\frac{a}{b}\right)^4\sin^2\phi\right)\right)\right]. \tag{C.15}$$

Then, in this coordinate system the Minkowski Tensors are diagonal with components

$$W_1^{0,2}|_{ii} = bc\int_0^{2\pi}{\rm d}\phi\int_0^{\pi}{\rm d}\theta\sin\theta\,\ell(\theta,\phi)\,\hat{n}_i^2, \tag{C.16}$$

$$W_2^{0,2}|_{ii} = bc\int_0^{2\pi}{\rm d}\phi\int_0^{\pi}{\rm d}\theta\sin\theta\,\ell(\theta,\phi)\,G_2\,\hat{n}_i^2. \tag{C.17}$$

For the ellipsoidal connected components described in the previous subsection, we can write the axis constants (a, b, c) in terms of the random variables $\nu_{\rm pk}, x, e, p$ according to

$$a^2 = \frac{6(\nu_{\rm pk}-\nu)}{x(1+3e+p)}, \quad b^2 = \frac{6(\nu_{\rm pk}-\nu)}{x(1-2p)}, \quad c^2 = \frac{6(\nu_{\rm pk}-\nu)}{x(1-3e+p)}. \tag{C.18}$$

JCAP08(2026)082

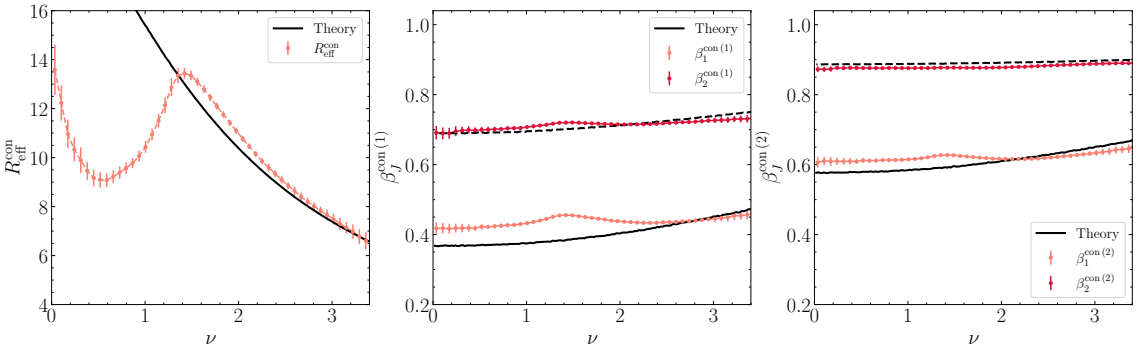


Figure 12. Comparison between measurements of $R_{\rm eff}^{\rm con}$, $\beta_J^{\rm con,cav\,(1)}$ and $\beta_J^{\rm con,cav\,(2)}$ (red points/error bars) extracted from $N = 50$ Gaussian random fields and the theoretical predictions derived in appendix C (black solid curves).

The shape statistics, for a single excursion subset are $\beta_J^{\rm con\,(1)} = W_1^{0,2}|_{JJ}/W_1^{0,2}|_{xx}$, and $\beta_J^{\rm con\,(2)} = W_2^{0,2}|_{JJ}/W_2^{0,2}|_{xx}$. The ensemble averages of the shape variables $\beta_J^{\rm con\,(1,2)}$ are:

$$\langle\beta_J^{\rm con\,(1,2)}\rangle = \frac{1}{N}\int {\rm d}e\,{\rm d}p\,\beta_J^{\rm con\,(1,2)}(e,p)\mathcal{J}(e,p)\int_0^\infty {\rm d}x\,\Theta(x,e,p)\,e^{-Q_{ep}(x,e,p)}x^8\int_\nu^\infty {\rm d}\nu' e^{-Q_{\nu x}(\nu',x)},$$
$$N = \int {\rm d}e\,{\rm d}p\,\mathcal{J}(e,p)\int_0^\infty {\rm d}x\,\Theta(x,e,p)\,e^{-Q_{ep}(x,e,p)}x^8\int_\nu^\infty {\rm d}\nu' e^{-Q_{\nu x}(\nu',x)}. \qquad \text{(C.19)}$$

All components of $\beta_J^{\rm con\,(1,2)}$ can be written purely in terms of axis ratios a/b and a/c, and hence do not contain explicit x, $\nu_{\rm pk}$ or ν dependence. However, ν and x still enter the ensemble averages due to the fact that they are correlated via the $\exp[-Q_{\nu x}]$ term, and x, e and p are subsequently correlated through $\exp[-Q_{ep}(x,e,p)]$ after ν has been marginalised over.

In figure 12 we present measurements of $R_{\rm eff}^{\rm con}$ (left panel), $\beta_J^{\rm con\,(1)}$ (middle panel) and $\beta_J^{\rm con\,(2)}$ (right panel) for the Gaussian random fields considered in section 3 (cf. red curves, lower panels of figure 1). The black solid/dashed curves are the theoretical ensemble averages constructed in this section. We find good agreement for $\nu \gtrsim 2.5$, as expected. The numerical measurements of $R_{\rm eff}^{\rm con}$ (cf. red points, left panel) rise faster than the theoretical prediction, due to the presence of peak-saddle chains that have not been accounted for in our simple analytic prescription.

The theoretical prediction does not exactly match $\beta_J^{\rm con\,(1)}$ or $\beta_J^{\rm con\,(2)}$ at high thresholds, with the black solid/dashed curves lying above the numerical results. This is due to a numerical systematic, which slightly reduces the isotropy of the connected components. Small, pixel-scale objects will be present at all thresholds, and these objects will exhibit spurious anisotropy due to the fact that they are not well resolved. This systematic presents a larger impact on $\beta_J^{\rm con\,(1)}$ and $\beta_J^{\rm con\,(2)}$ than dimension-full quantities such as $R_{\rm eff}^{\rm con}$, because barely resolved objects will be naturally down-weighted by their size in the $R_{\rm eff}^{\rm con}$ average. One could apply minimum size cuts to mitigate this numerical artifact.

So far in this appendix, we have used an ellipsoidal approximation in the vicinity of a peak to estimate the morphological properties of connected components. In figure 13 we present an alternative perspective, specifically we plot the dimensionless quantity $R_{\rm eff}^{\rm con}/r_c$ over the range $0 \leq \nu \leq 3.5$ for a Gaussian random field in real space with the fiducial ΛCDM

JCAP08(2026)082

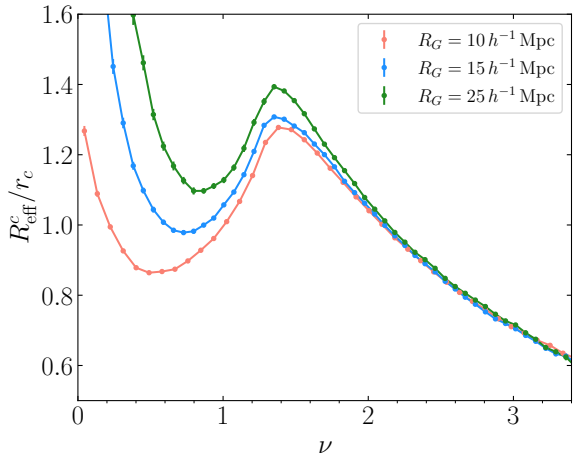


Figure 13. Measurements of $R^{\rm con}_{\rm eff}/r_c$ for $N = 50$ realisations of Gaussian random fields, smoothed on scales $R_G = 10, 15, 25\,h^{-1}$ Mpc (red/blue/green points/errorbars).

power spectrum from the main body of the text, where $r_c = \sigma_0/\sigma_1$. The red/blue/green points/error bars are the mean/error on mean of $N_{\rm real} = 50$ realisations of random fields smoothed on scales $R_G = 10, 15, 25\,h^{-1}$ Mpc respectively. We find that for $\nu \gtrsim 2$, the curves are practically indistinguishable. This indicates that to high precision, the statistic $R^{\rm con}_{\rm eff}$ can be described purely in terms of the correlation length of the field, r_c and some function of ν at these thresholds.

Contrarily, at $\nu \lesssim 2$, $R^{\rm con}_{\rm eff}/r_c$ shows dependence on the smoothing scale R_G, with smaller scale smoothing dropping lower before finally rising at $\nu \sim 0$. This indicates that a higher number of small sized connected components survive after the large objects form at the peak $\nu \sim 1.4$ when we smooth with a smaller scale. In this regime $0 < \nu \lesssim 1.4$, the shape of the curve contains information on the percolation behaviour of the field. For $\nu \sim 0$, the rising behaviour common to all three curves is due to the smaller substructures combining with the single large excursion subset.

In terms of the ensemble average discussion in this section, for $\nu \gtrsim 2$ the similarity of the curves suggests that the average morphology of the excursion sets is dominated by the local shape of the field encoded in r_c. This implies that we can approximately express $\langle R^{\rm con}_{\rm eff}\rangle$ purely in terms of an integral of the joint PDF $P(\delta, \nabla\delta, \nabla\nabla\delta)$ at a single point in the space, similarly to the Minkowski Functionals. The curves start to deviate from one another at $\nu \lesssim 2$, approximately where loops start to significantly contribute to the genus in the form of the Betti number b_1.

References

[1] P.J.E. Peebles, *The large-scale structure of the universe*, Princeton University Press (1980).

[2] F. Bernardeau, S. Colombi, E. Gaztañaga and R. Scoccimarro, *Large-scale structure of the Universe and cosmological perturbation theory*, *Phys. Rep.* **367** (2002) 1 [astro-ph/0112551] [INSPIRE].

[3] K.R. Mecke, T. Buchert and H. Wagner, *Robust morphological measures for large-scale structure in the Universe*, *Astron. Astrophys.* **288** (1994) 697 [astro-ph/9312028] [INSPIRE].

JCAP08(2026)082

[4] J. Schmalzing, M. Kerscher and T. Buchert, *Minkowski functionals in cosmology*, *Proc. Int. Sch. Phys. Fermi* **132** (1996) 281 [astro-ph/9508154] [INSPIRE].

[5] G. Schroder-Turk et al., *Tensorial Minkowski functionals and anisotropy measures for planar patterns*, *J. Microsc.* **238** (2010) 57.

[6] T. Matsubara and B. Jain, *The topology of weak lensing fields*, *Astrophys. J.* **552** (2001) L89 [astro-ph/0009402] [INSPIRE].

[7] G.E. Schröder-Turk et al., *Minkowski tensors of anisotropic spatial structure*, *New J. Phys.* **15** (2013) 083028 [arXiv:1009.2340].

[8] T. Matsubara and J. Yokoyama, *Genus Statistics of the Large-Scale Structure with Non-Gaussian Density Fields*, *Astrophys. J.* **463** (1996) 409 [astro-ph/9509086] [INSPIRE].

[9] C. Hikage, E. Komatsu and T. Matsubara, *Primordial Non-Gaussianity and Analytical Formula for Minkowski Functionals of the Cosmic Microwave Background and Large-scale Structure*, *Astrophys. J.* **653** (2006) 11 [astro-ph/0607284] [INSPIRE].

[10] P. Chingangbam and C. Park, *Statistical nature of non-Gaussianity from cubic order primordial perturbations: CMB map simulations and genus statistic*, *JCAP* **12** (2009) 019 [arXiv:0908.1696] [INSPIRE].

[11] C. Park et al., *Betti numbers of Gaussian fields*, *J. Korean Astron. Soc.* **46** (2013) 125 [arXiv:1307.2384] [INSPIRE].

[12] C. Blake, J.B. James and G.B. Poole, *Using the topology of large-scale structure in the WiggleZ Dark Energy Survey as a cosmological standard ruler*, *Mon. Not. Roy. Astron. Soc.* **437** (2014) 2488 [arXiv:1310.6810] [INSPIRE].

[13] R. Speare, J.R. Gott, J. Kim and C. Park, *Horizon Run 3: Topology as a Standard Ruler*, *Astrophys. J.* **799** (2015) 176 [arXiv:1310.4278] [INSPIRE].

[14] A.L. Melott, *The topology of large-scale structure in the universe*, *Phys. Rep.* **193** (1990) 1.

[15] W.N. Colley et al., *Topology from the simulated Sloan Digital Sky Survey*, *Astrophys. J.* **529** (2000) 795 [astro-ph/9902332] [INSPIRE].

[16] J.R. Gott III et al., *Genus topology of structure in the sloan digital sky survey: Model testing*, *Astrophys. J.* **675** (2008) 16 [astro-ph/0610762] [INSPIRE].

[17] Y.-Y. Choi et al., *Galaxy Clustering Topology in the Sloan Digital Sky Survey Main Galaxy Sample: a Test for Galaxy Formation Models*, *Astrophys. J. Suppl.* **190** (2010) 181 [arXiv:1005.0256] [INSPIRE].

[18] S.A. Appleby et al., *Cosmological Parameter Estimation from the Two-Dimensional Genus Topology — Measuring the Shape of the Matter Power Spectrum*, *Astrophys. J.* **896** (2020) 145 [arXiv:2004.01424] [INSPIRE].

[19] C. Hikage et al., *Limits on Primordial Non-Gaussianity from Minkowski Functionals of the WMAP Temperature Anisotropies*, *Mon. Not. Roy. Astron. Soc.* **389** (2008) 1439 [arXiv:0802.3677] [INSPIRE].

[20] C.P. Novaes, A. Bernui, G.A. Marques and I.S. Ferreira, *Local analyses of Planck maps with Minkowski Functionals*, *Mon. Not. Roy. Astron. Soc.* **461** (2016) 1363 [arXiv:1606.04075] [INSPIRE].

[21] P. Chingangbam, V. Ganesan, K.P. Yogendran and C. Park, *On Minkowski Functionals of CMB polarization*, *Phys. Lett. B* **771** (2017) 67 [arXiv:1705.04454] [INSPIRE].

[22] Planck collaboration, *Planck 2018 results. VII. Isotropy and Statistics of the CMB*, *Astron. Astrophys.* **641** (2020) A7 [arXiv:1906.02552] [INSPIRE].

JCAP08(2026)082

[23] S. Appleby et al., *Minkowski Functionals of SDSS-III BOSS: Hints of Possible Anisotropy in the Density Field?*, *Astrophys. J.* **928** (2022) 108 [arXiv:2110.06109] [INSPIRE].

[24] J.R. Gott III et al., *Topology of microwave background fluctuations: Theory*, *Astrophys. J.* **352** (1990) 1.

[25] C. Park and J.R. Gott, *Dynamical evolution of topology of large-scale structure*, *Astrophys. J.* **378** (1991) 457.

[26] J. Schmalzing and T. Buchert, *Beyond genus statistics: A Unifying approach to the morphology of cosmic structure*, *Astrophys. J.* **482** (1997) L1 [astro-ph/9702130] [INSPIRE].

[27] J. Schmalzing and K.M. Gorski, *Minkowski functionals used in the morphological analysis of cosmic microwave background anisotropy maps*, *Mon. Not. Roy. Astron. Soc.* **297** (1998) 355 [astro-ph/9710185] [INSPIRE].

[28] A.L. Melott et al., *Topology of large-scale structure. IV — Topology in two dimensions*, *Astrophys. J.* **345** (1989) 618.

[29] C. Park, J.R. Gott III, A.L. Melott and I.D. Karachentsev, *The Topology of Large-Scale Structure. VI. Slices of the Universe*, *Astrophys. J.* **387** (1992) 1 [INSPIRE].

[30] M. Kerscher, J. Schmalzing, T. Buchert and H. Wagner, *Fluctuations in the IRAS 1.2 Jy catalog*, *Astron. Astrophys.* **333** (1998) 1 [astro-ph/9704028] [INSPIRE].

[31] C. Park, J.R. Gott III and Y.J. Choi, *Topology of the galaxy distribution in the Hubble deep fields*, *Astrophys. J.* **553** (2001) 33 [astro-ph/0008353] [INSPIRE].

[32] C. Park and Y.-R. Kim, *Large-Scale Structure of the Universe as a Cosmic Standard Ruler*, *Astrophys. J. Lett.* **715** (2010) L185 [arXiv:0905.2268] [INSPIRE].

[33] C. Zunckel, J.R. Gott III and R. Lunnan, *Using the topology of large-scale structure to constrain dark energy*, *Mon. Not. Roy. Astron. Soc.* **412** (2011) 1402 [arXiv:1005.3631] [INSPIRE].

[34] V. Sahni, B.S. Sathyaprakash and S.F. Shandarin, *Shapefinders: A New shape diagnostic for large scale structure*, *Astrophys. J. Lett.* **495** (1998) L5 [astro-ph/9801053] [INSPIRE].

[35] S. Bharadwaj et al., *Evidence for filamentarity in the las campanas redshift survey*, *Astrophys. J.* **528** (2000) 21 [astro-ph/9904406] [INSPIRE].

[36] T. Matsubara, *Statistics of Smoothed Cosmic Fields in Perturbation Theory. I. Formulation and Useful Formulae in Second-Order Perturbation Theory*, *Astrophys. J.* **584** (2003) 1 [INSPIRE].

[37] R. van de Weygaert et al., *Probing Dark Energy with Alpha Shapes and Betti Numbers*, arXiv:1110.5528 [INSPIRE].

[38] R. van de Weygaert et al., *Alpha, Betti and the Megaparsec Universe: on the Topology of the Cosmic Web*, *Trans. Comput. Sci.* **14** (2011) 60 [arXiv:1306.3640] [INSPIRE].

[39] P. Chingangbam and C. Park, *Residual foreground contamination in the WMAP data and bias in non-Gaussianity estimation*, *JCAP* **02** (2013) 031 [arXiv:1210.2250] [INSPIRE].

[40] N. Shivshankar et al., *Felix: A Topology based Framework for Visual Exploration of Cosmic Filaments*, *IEEE Trans. Visual Comput. Graphics* **22** (2015) 1745 [arXiv:1508.00737] [INSPIRE].

[41] P. Pranav et al., *The Topology of the Cosmic Web in Terms of Persistent Betti Numbers*, *Mon. Not. Roy. Astron. Soc.* **465** (2017) 4281 [arXiv:1608.04519] [INSPIRE].

[42] P. Pranav et al., *Unexpected Topology of the Temperature Fluctuations in the Cosmic Microwave Background*, *Astron. Astrophys.* **627** (2019) A163 [arXiv:1812.07678] [INSPIRE].

[43] P. Pranav et al., *Topology and Geometry of Gaussian random fields I: on Betti Numbers, Euler characteristic and Minkowski functionals*, *Mon. Not. Roy. Astron. Soc.* **485** (2019) 4167 [arXiv:1812.07310] [INSPIRE].

JCAP08(2026)082

[44] J. Feldbrugge et al., *Stochastic Homology of Gaussian vs. non-Gaussian Random Fields: Graphs towards Betti Numbers and Persistence Diagrams*, *JCAP* **09** (2019) 052 [arXiv:1908.01619] [INSPIRE].

[45] G. Wilding et al., *Persistent homology of the cosmic web — I. Hierarchical topology in ΛCDM cosmologies*, *Mon. Not. Roy. Astron. Soc.* **507** (2021) 2968 [arXiv:2011.12851] [INSPIRE].

[46] D. Munshi et al., *Morphology of weak lensing convergence maps*, *Mon. Not. Roy. Astron. Soc.* **507** (2021) 1421 [arXiv:2010.05669] [INSPIRE].

[47] W. Liu, A. Jiang and W. Fang, *Probing massive neutrinos with the Minkowski functionals of large-scale structure*, *JCAP* **07** (2022) 045 [arXiv:2204.02945] [INSPIRE].

[48] W. Liu, A. Jiang and W. Fang, *Probing massive neutrinos with the Minkowski functionals of the galaxy distribution*, *JCAP* **09** (2023) 037 [arXiv:2302.08162] [INSPIRE].

[49] W. Liu et al., *Cosmological constraints from the Minkowski functionals of the BOSS CMASS galaxy sample*, *JCAP* **05** (2025) 064 [arXiv:2501.01698] [INSPIRE].

[50] S. Rana, T. Ghosh, J.S. Bagla and P. Chingangbam, *Non-Gaussianity of diffuse Galactic synchrotron emission at* 408 *MHz*, *Mon. Not. Roy. Astron. Soc.* **481** (2018) 970 [arXiv:1806.01565] [INSPIRE].

[51] F. Rahman, P. Chingangbam and T. Ghosh, *The nature of non-Gaussianity and statistical isotropy of the* 408 *MHz Haslam synchrotron map*, *JCAP* **07** (2021) 026 [arXiv:2104.00419] [INSPIRE].

[52] M.H.J. Kanafi and S.M.S. Movahed, *Probing the Anisotropy and Non-Gaussianity in the Redshift Space through the Conditional Moments of the First Derivative*, *Astrophys. J.* **963** (2024) 31 [arXiv:2308.03086] [INSPIRE].

[53] A. Afzal, M. Alakhras, M.H.J. Kanafi and S.M.S. Movahed, *Cosmic strings-induced CMB anisotropies in light of weighted morphology*, *Mon. Not. Roy. Astron. Soc.* **541** (2025) 3851 [arXiv:2503.00758] [INSPIRE].

[54] S. Alesker, *Description of Continuous Isometry Covariant Valuations on Convex Sets*, *Geom. Dedicata* **74** (1999) 241.

[55] C. Beisbart, R. Valdarnini and T. Buchert, *The morphological and dynamical evolution of simulated galaxy clusters*, *Astron. Astrophys.* **379** (2001) 412 [astro-ph/0109459] [INSPIRE].

[56] C. Beisbart, T. Buchert and H. Wagner, *Morphometry of spatial patterns*, *Physica A* **293** (2001) 592 [astro-ph/0007459] [INSPIRE].

[57] C. Beisbart, R. Dahlke, K. Mecke and H. Wagner, *Vector- and Tensor-Valued Descriptors for Spatial Patterns*, in *Morphology of Condensed Matter*, *Lecture Notes in Physics* **600**, Springer Verlag, Berlin, Germany (2002), p. 238–260 [DOI:10.1007/3-540-45782-8_10].

[58] D. Hug, R. Schneider and R. Schuster, *Integral geometry of tensor valuations*, *Adv. Appl. Math.* **41** (2008) 482.

[59] P. Chingangbam et al., *Tensor Minkowski Functionals for random fields on the sphere*, *JCAP* **12** (2017) 023 [arXiv:1707.04386] [INSPIRE].

[60] S. Appleby, J.P. Kochappan, P. Chingangbam and C. Park, *Ensemble Average of Three-Dimensional Minkowski Tensors of a Gaussian Random Field in Redshift Space*, *Astrophys. J.* **887** (2019) 128 [arXiv:1908.02440] [INSPIRE].

[61] P. Chingangbam, P. Goyal, K.P. Yogendran and S. Appleby, *Geometrical meaning of statistical isotropy of smooth random fields in two dimensions*, *Phys. Rev. D* **104** (2021) 123516 [arXiv:2109.05726] [INSPIRE].

[62] M.A. Klatt, M. Hörmann and K. Mecke, *Characterization of Anisotropic Gaussian Random Fields by Minkowski Tensors*, *J. Stat. Mech.* **2022** (2022) 043301 [arXiv:2111.13349].

JCAP08(2026)082

[63] S. Appleby et al., *Minkowski Tensors in Two Dimensions: Probing the Morphology and Isotropy of the Matter and Galaxy Density Fields*, *Astrophys. J.* **858** (2018) 87 [arXiv:1712.07466] [INSPIRE].

[64] F.M. Schaller, J. Wagner and S.C. Kapfer, *papaya2: 2D Irreducible Minkowski Tensor computation*, *J. Open Source Softw.* **5** (2020) 2538.

[65] C. Collischon et al., *Morphometry on the sphere: Cartesian and irreducible Minkowski tensors explained and implemented*, *Commun. Phys.* **7** (2024) 254 [arXiv:2402.06286] [INSPIRE].

[66] V. Ganesan and P. Chingangbam, *Tensor Minkowski Functionals: first application to the CMB*, *JCAP* **06** (2017) 023 [arXiv:1608.07452] [INSPIRE].

[67] P.K. Joby et al., *Search for anomalous alignments of structures in Planck data using Minkowski Tensors*, *JCAP* **01** (2019) 009 [arXiv:1807.01306] [INSPIRE].

[68] J.P. Kochappan et al., *Application of the contour Minkowski tensor and $\mathcal{D}$ statistic to the Planck E-mode data*, *Phys. Rev. D* **103** (2021) 123523 [arXiv:2106.05757] [INSPIRE].

[69] P. Goyal, P. Chingangbam and S. Appleby, *Morphology of CMB fields — effect of weak gravitational lensing*, *JCAP* **02** (2020) 020 [arXiv:1911.04740] [INSPIRE].

[70] P. Goyal and P. Chingangbam, *Local patch analysis for testing statistical isotropy of the Planck convergence map*, *JCAP* **08** (2021) 006 [arXiv:2104.00418] [INSPIRE].

[71] A. Kapahtia, P. Chingangbam and S. Appleby, *Morphology of 21 cm brightness temperature during the Epoch of Reioinization using Contour Minkowski Tensor*, *JCAP* **09** (2019) 053 [arXiv:1904.06840] [INSPIRE].

[72] A. Kapahtia et al., *Prospects of constraining reionization model parameters using Minkowski tensors and Betti numbers*, *JCAP* **05** (2021) 026 [arXiv:2101.03962] [INSPIRE].

[73] F. Rahman, P. Chingangbam and T. Ghosh, *Statistical properties of galactic synchrotron temperature and polarization maps — a multi-frequency comparison*, *JCAP* **01** (2024) 036 [arXiv:2212.06076] [INSPIRE].

[74] S. Appleby et al., *Minkowski Tensors in Three Dimensions: Probing the Anisotropy Generated by Redshift Space Distortion*, *Astrophys. J.* **863** (2018) 200 [arXiv:1805.08752] [INSPIRE].

[75] A.G. Doroshkevich, Y.B. Zeldovich, R.A. Syunyaev and M.Y. Khlopov, *Astrophysical implications of the neutrino rest mass. II. The density-perturbation spectrum and small-scale fluctuations in the microwave background*, *Pisma Astron. Zh.* **6** (1980) 457 [*Sov. Astron. Lett.* **6** (1980) 252] [INSPIRE].

[76] A.G. Doroshkevich, Y.B. Zeldovich, R.A. Syunyaev and M.Y. Khlopov, *Astrophysical Implications of the Neutrino Rest Mass. III. Nonlinear Growth of Perturbations and the Missing Mass*, *Sov. Astron. Lett.* **6** (1980) 257 [INSPIRE].

[77] A.G. Doroshkevich et al., *Cosmological impact of the neutrino rest mass*, *Ann. N. Y. Acad. Sci.* **375** (1981) 32.

[78] Y.-R. Kim et al., *Systematic effects on the genus topology of the large-scale structure of the universe*, *Astrophys. J. Suppl.* **212** (2014) 22 [arXiv:1404.6314] [INSPIRE].

[79] J. Kim, C. Park, B. L'Huillier and S.E. Hong, *Horizon Run 4 Simulation: Coupled Evolution of Galaxies and Large-scale Structures of the Universe*, *J. Korean Astron. Soc.* **48** (2015) 213 [arXiv:1508.05107] [INSPIRE].

[80] S. Appleby, C. Park, S.E. Hong and J. Kim, *Topology of Large-Scale Structures of Galaxies in Two Dimensions — Systematic Effects*, *Astrophys. J.* **836** (2017) 45 [arXiv:1702.04511] [INSPIRE].

[81] G.A. Marques et al., *Constraining neutrino mass with weak lensing Minkowski Functionals*, *JCAP* **06** (2019) 019 [arXiv:1812.08206] [INSPIRE].

JCAP08(2026)082

[82] Y. Liu, Y. Yu, H.-R. Yu and P. Zhang, *Neutrino effects on the morphology of cosmic large-scale structure*, *Phys. Rev. D* **101** (2020) 063515 [arXiv:2002.08846] [INSPIRE].

[83] F. Villaescusa-Navarro et al., *The Quijote simulations*, *Astrophys. J. Suppl.* **250** (2020) 2 [arXiv:1909.05273] [INSPIRE].

[84] M. Zennaro et al., *Initial Conditions for Accurate N-Body Simulations of Massive Neutrino Cosmologies*, *Mon. Not. Roy. Astron. Soc.* **466** (2017) 3244 [arXiv:1605.05283] [INSPIRE].

[85] P. Chingangbam, *On the statistical nature of Betti numbers and Euler characteristic of smooth random fields*, arXiv:2507.06255 [INSPIRE].

[86] S. Appleby, J.P. Kochappan, P. Chingangbam and C. Park, *Minkowski Tensors in Redshift Space — Beyond the Plane-parallel Approximation*, *Astrophys. J.* **942** (2023) 110 [arXiv:2208.10164] [INSPIRE].

[87] H. Tomita, *Curvature Invariants of Random Interface Generated by Gaussian Fields*, *Prog. Theor. Phys.* **76** (1986) 952.

[88] T. Sousbie, C. Pichon and H. Kawahara, *The persistent cosmic web and its filamentary structure — II. Illustrations*, *Mon. Not. Roy. Astron. Soc.* **414** (2011) 384 [arXiv:1009.4014] [INSPIRE].

[89] P. Chingangbam, C. Park, K.P. Yogendran and R. van de Weygaert, *Hot and Cold Spot Counts as Probes of Non-Gaussianity in the Cosmic Microwave Background*, *Astrophys. J.* **755** (2012) 122 [arXiv:1206.0436] [INSPIRE].

[90] P. Pranav, *Topology and geometry of Gaussian random fields II: on critical points, excursion sets, and persistent homology*, arXiv:2109.08721 [INSPIRE].

[91] C. Park, J.R. Gott III and L.N. da Costa, *Large-scale structure in the Southern Sky Redshift Survey*, *Astrophys. J. Lett.* **392** (1992) L51.

[92] C. Park, J. Kim and J.R. Gott III, *Effects of gravitational evolution, biasing, and redshift space distortion on topology*, *Astrophys. J.* **633** (2005) 1 [astro-ph/0503584] [INSPIRE].

[93] D. Pogosyan, C. Gay and C. Pichon, *Invariant joint distribution of a stationary random field and its derivatives: Euler characteristic and critical point counts in* 2 *and* 3*D*, *Phys. Rev. D* **80** (2009) 081301 [*Erratum ibid.* **81** (2010) 129901] [arXiv:0907.1437] [INSPIRE].

[94] T. Matsubara, C. Hikage and S. Kuriki, *Minkowski functionals and the nonlinear perturbation theory in the large-scale structure: Second-order effects*, *Phys. Rev. D* **105** (2022) 023527 [arXiv:2012.00203] [INSPIRE].

[95] J.R. Gott III, D.H. Weinberg and A.L. Melott, *A quantitative approach to the topology of large-scale structure*, *Astrophys. J.* **319** (1987) 1.

[96] D.H. Weinberg, J.R. Gott III and A.L. Melott, *The topology of large-scale structure. I — Topology and the random phase hypothesis*, *Astrophys. J.* **321** (1987) 2.

[97] A.L. Melott, D.H. Weinberg and J.R. Gott III, *The topology of large-scale structure. II — Nonlinear evolution of Gaussian models*, *Astrophys. J.* **328** (1988) 50.

[98] N. Kaiser, *Clustering in real space and in redshift space*, *Mon. Not. Roy. Astron. Soc.* **227** (1987) 1 [INSPIRE].

[99] A.J.S. Hamilton, *Linear redshift distortions: A Review*, in *The Evolving Universe*, *Astrophysics and Space Science Library* **231**, D. Hamilton ed., Springer, Dordrecht, Netherlands (1998), p. 185–275 [DOI:10.1007/978-94-011-4960-0_17] [astro-ph/9708102] [INSPIRE].

[100] J.C. Jackson, *A critique of Rees's theory of primordial gravitational radiation*, *Mon. Not. Roy. Astron. Soc.* **156** (1972) 1P [arXiv:0810.3908] [INSPIRE].

[101] T. Matsubara, *Statistics of isodensity contours in redshift space*, *Astrophys. J.* **457** (1996) 13 [astro-ph/9501055] [INSPIRE].

JCAP08(2026)082

[102] S. Appleby et al., *Non-Gaussian Expansion of Minkowski Tensors in Redshift Space*, *Astrophys. J.* **1001** (2026) 213 [arXiv:2507.10091] [INSPIRE].

[103] W. Liu et al., *Probing massive neutrinos and modified gravity with redshift-space morphologies and anisotropies of large-scale structure*, *JCAP* **04** (2025) 088 [arXiv:2412.05662] [INSPIRE].

[104] KATRIN collaboration, *Direct neutrino-mass measurement based on 259 days of KATRIN data*, *Science* **388** (2025) 180 [arXiv:2406.13516] [INSPIRE].

[105] PLANCK collaboration, *Planck 2018 results. VI. Cosmological parameters*, *Astron. Astrophys.* **641** (2020) A6 [*Erratum ibid.* **652** (2021) C4] [arXiv:1807.06209] [INSPIRE].

[106] DESI collaboration, *DESI 2024 VI: cosmological constraints from the measurements of baryon acoustic oscillations*, *JCAP* **02** (2025) 021 [arXiv:2404.03002] [INSPIRE].

[107] T. Sousbie, *The persistent cosmic web and its filamentary structure I: Theory and implementation*, *Mon. Not. Roy. Astron. Soc.* **414** (2011) 350 [arXiv:1009.4015] [INSPIRE].

[108] M. Aggarwal et al., *Topological Approach to Void Finding Applied to the SDSS Galaxy Map*, *Astrophys. J.* **975** (2024) 95 [arXiv:2409.01905] [INSPIRE].

[109] C. Hahn and F. Villaescusa-Navarro, *Constraining M_ν with the bispectrum. Part II. The information content of the galaxy bispectrum monopole*, *JCAP* **04** (2021) 029 [arXiv:2012.02200] [INSPIRE].

[110] Z. Zheng, A.L. Coil and I. Zehavi, *Galaxy Evolution from Halo Occupation Distribution Modeling of DEEP2 and SDSS Galaxy Clustering*, *Astrophys. J.* **667** (2007) 760 [astro-ph/0703457] [INSPIRE].

[111] J. Liu and M.S. Madhavacheril, *Constraining neutrino mass with the tomographic weak lensing one-point probability distribution function and power spectrum*, *Phys. Rev. D* **99** (2019) 083508 [arXiv:1809.10747] [INSPIRE].

[112] J.M. Bardeen, J.R. Bond, N. Kaiser and A.S. Szalay, *The Statistics of Peaks of Gaussian Random Fields*, *Astron. J.* **304** (1986) 15.

[113] S. Codis et al., *Non-Gaussian Minkowski functionals & extrema counts in redshift space*, *Mon. Not. Roy. Astron. Soc.* **435** (2013) 531 [arXiv:1305.7402] [INSPIRE].

[114] C. Germani, M.A. Gorji, M. Uwabo-Niibo and M. Yamaguchi, *Peaks sphericity of non-Gaussian random fields*, *JCAP* **09** (2025) 052 [arXiv:2503.05434] [INSPIRE].

JCAP08(2026)082